



# A regularized variational mechanics theory for modeling the evolution of brittle crack networks in composite materials with sharp interfaces<sup>☆</sup>

Kaushik Vijaykumar<sup>a</sup>, Benjamin E. Grossman-Ponemon<sup>a,1</sup>, Yang Wan<sup>a</sup>,  
Pooya Yousefi<sup>b,2</sup>, Christopher J. Larsen<sup>b</sup>, Haneesh Kesari<sup>a,\*</sup>

<sup>a</sup> Division of Solid Mechanics, School of Engineering, Brown University, Providence, RI 02912, United States

<sup>b</sup> Department of Mathematical Sciences, Worcester Polytechnic Institute, Worcester, MA 01609, United States

## ARTICLE INFO

### Keywords:

Regularized variational fracture theory  
Weak interface  
Interfacial fracture

## ABSTRACT

In the design of structural materials, there is traditionally a tradeoff between achieving high strength and achieving high toughness. Nature offers creative solutions to this problem in the form of structural biomaterials (SBs), intelligent arrangements of mineral and organic phases which possess greater strength and toughness than the constituents. The micro-architecture of SBs like nacre and sea sponge spicules are characterized by weak organic interfaces between brittle mineral phases. To better understand the toughening mechanisms in SBs requires simulation techniques which can resolve arbitrary interface and bulk fracture patterns.

In this work, we present a modified regularization of Variational Fracture Theory (VFT) that allows for simulation of fracture in materials and structures with weak interfaces. The core of our approach is to widen the weak interfaces on a length scale proportional to that of the diffuse damage field, and assign a reduced fracture toughness therein. We show that in 2D the modified regularized functionals  $\Gamma$ -converge to that for sharp cracks. The resulting thin weak interfaces have fracture toughness which depends on the bulk material fracture toughness, the widened interface fracture toughness, and the ratio of the widened interface length scale to the crack regularization length scale. We next apply our modified regularization within a computer implementation of regularized VFT, which we term RVFTI. We assess the performance of RVFTI in 2D by reproducing the effective interface fracture toughness predicted by the  $\Gamma$ -convergence theory and simulating crack trapping at a bi-material interface. We then use RVFTI to study toughening in SB-inspired microarchitectures, namely layered materials and materials with wavy interfaces.

## 1. Introduction

In structural engineering, it is important for materials to possess both high strength and high toughness. However, in conventional structural materials such as steels and aluminum alloys, strength and toughness are in competition, as the mechanisms that enhance

<sup>☆</sup> This research paper is dedicated to Professor Allan Bower on the occasion of his retirement. We celebrate him for his exceptional and deep scholarship in the field of Solid Mechanics, and for inspiring and supporting several young scientists through his mentorship and teaching.

\* Corresponding author.

E-mail address: [haneesh\\_kesari@brown.edu](mailto:haneesh_kesari@brown.edu) (H. Kesari).

<sup>1</sup> New address: Department of Physics and Engineering, John Carroll University, University Heights, OH, 44118, United States.

<sup>2</sup> New address: Department of Mathematics & Statistics, McMaster University, Hamilton, Ontario, L8S 4K1, Canada.

<https://doi.org/10.1016/j.jmps.2024.105772>

Received 16 November 2023; Received in revised form 30 May 2024; Accepted 4 July 2024

Available online 16 August 2024

0022-5096/© 2024 Elsevier Ltd. All rights are reserved, including those for text and data mining, AI training, and similar technologies.

one can inhibit the other (Ritchie, 2011). Recent studies indicate that structural biomaterials (SBs) show both high strength and toughness (Ritchie, 2011; Barthelat and Espinosa, 2007; Barthelat and Rabiei, 2011; Currey, 1977; Rabiei et al., 2012). Most such SBs are heterogeneous in nature and consist of a mineral (stiff) phase and an organic (compliant) phase. Nacre is one such SB where the mineral phase occupies  $> 95\%$  of the volume fraction of the material (Barthelat and Rabiei, 2011). Due to the presence of high volume fraction of the mineral phase, Aragonite ( $\text{CaCO}_3$ ), the bulk properties of nacre such as Young's modulus and Poisson's ratio are almost identical to Aragonite. Hence, it is meaningful to compare the mechanical behavior of nacre to Aragonite. Nacre obtains its high strength properties from Aragonite, and has a tensile strength of  $\approx 170$  MPa which is almost identical to that of Aragonite (Jackson et al., 1988). However, the work of fracture in nacre can be as large as  $1500 \text{ J/m}^2$ , while that in Aragonite is about  $10 \text{ J/m}^2$  (Barthelat and Espinosa, 2007). Hence, SBs are ideal prototypical materials for understanding mechanisms which enable high strength and toughness.

The micro-architectural arrangement of phases varies in different SBs, although the organic phase is often located at interfaces in the mineral phase. Such an example is nacre, whose micro-architecture resembles a brick-and-mortar structure as seen in Fig. 1(a). Here, the bricks consist of the mineral phase while the mortar is organic. However, in other SBs such as spicules in sea sponges, some of the organic phase is also mixed with the mineral phase (Wang et al., 2010; Weaver et al., 2003; Neilson et al., 2014). The micro-architecture of spicules resembles that of a lamellar structure, as seen in Fig. 1(b), where the mineral phase is arranged concentrically and is separated by a nanometer-thin layer (approximately 35 nm Zlotnikov et al., 2013) of the organic phase.

Attempts to replicate these micro-architectural designs have been quite promising. As shown in Fig. 1(c), an alumina-based composite mimicking the micro-architecture of nacre achieved higher peak stress and exhibited greater area under the stress-strain curve, called the work of fracture (Tattersall and Tappin, 1966), when subjected to notched three-point bending experiments (Ritchie, 2011). The work of fracture is a useful measure of toughness in materials, as it quantifies the energy needed to be applied in order to break the structure. It can be clearly seen that the alumina-based composite has higher strength and toughness than nacre.

The superior toughness properties of SBs, such as bone and nacre, are plotted in Fig. 1(d). From the figure, we see that bone and nacre display higher toughness than either of their respective mineral and organic phases. Furthermore, the alumina-based composite has even higher toughness than the SBs. This suggests that a comprehensive understanding of the failure mechanisms in SBs can aid in designing materials with superior properties to those found in nature.

It has been postulated that higher toughness in SBs can be attributed to fracture mechanisms such as crack deflection and crack arrest, which are shown in Fig. 1(b) (Weaver et al., 2010; Barthelat and Rabiei, 2011). However, insights into the underlying toughening mechanisms such as the interplay of fracture mechanisms at different length scales and the operating extrinsic toughening mechanisms (e.g., crack deflection and crack arrest) have not been studied adequately. Further, the effect of model parameters such as the thickness of the interface, the ratio of fracture toughness of the phases, and the arrangement of the phases on the toughness of the SBs is still unexplored. To address these gaps, we believe that computational models capable of modeling such complex architectural designs can be used to conduct virtual experiments which can aid in engineering synthetic materials with both high strength and toughness.

In recent years, researchers have performed experimental and analytical studies to explore mechanisms to increase toughness in ceramic composites (Suresh, 1985; Clegg et al., 1990; Evans et al., 2001). Phenomena such as crack trapping and crack bridging due elastic heterogeneities and their ability to enhance the toughness of materials have also been studied (Lange, 1970; Bower and Ortiz, 1991; Mower and Argon, 1995; Xu et al., 1998). A perturbation-based analysis was employed to shed light on the role of elastic moduli on fracture toughness (Huajian, 1991). Studies predominantly using semi-analytical methods have investigated the toughness of interfaces in the presence of elastic heterogeneities in semi-infinite geometries (Comninou, 1977; Cook and Erdogan, 1972; Delale and Erdogan, 1988; He and Hutchinson, 1989; Hutchinson and Suo, 1991). However, these studies fall short in providing a complete description of how toughness is enhanced in SBs for various reasons:

- (1) The aforementioned numerical studies are limited to small extensions to the pre-defined crack in ceramic composites or SBs, and therefore the influence of crack tortuosity on toughness is unclear.
- (2) Fracture mechanisms such as crack bridging, crack deflection, and crack arrest are not well understood.
- (3) SBs such as bone have a hierarchical architecture, and there are different fracture mechanisms operating at different length scales. The aforementioned works do not study the contributions of different mechanisms to the bulk toughening.
- (4) The influence of geometric features and micro-architecture on toughness is inadequately studied. Therefore, greater research is needed to understand these micro-architectures and how they might enhance both strength and toughness.

Numerical methods featuring cohesive zone models have been used to study how toughness can be enhanced in the presence of interfaces (Tvergaard and Hutchinson, 1996; Zavattieri et al., 2007). These studies are limited by the fact that cracks could only grow along a set of pre-defined paths, and therefore instabilities such as crack jumps from the interface to the bulk could not be simulated. Meanwhile, Begley and co-workers (Pro et al., 2015; Lim et al., 2016) simulated brick-and-mortar micro-architectures using rigid bricks and cohesive interfaces. The problem was solved using Monte Carlo methods by prescribing displacements to the bricks and iterating until a configuration with minimum energy is achieved.

Working in the broader realm of heterogeneous materials, Bourdin and Battacharya and collaborators (Hossain et al., 2014; Hsueh et al., 2018; Brach et al., 2019; Brodnik et al., 2020, 2021) have investigated through computations using regularized variational fracture theory (RVFT) (and in some cases with experiments) how the effective toughness of a specimen is affected by the presence of elastic heterogeneities and fracture toughness heterogeneities. In particular, the simulations were able to capture crack tortuosity which resulted from the geometry of the heterogeneities. These studies have generally focused on evaluating the effective fracture toughness in domains with periodic arrangements of stiff and compliant materials subjected to Mode-I loading. Further, the effective

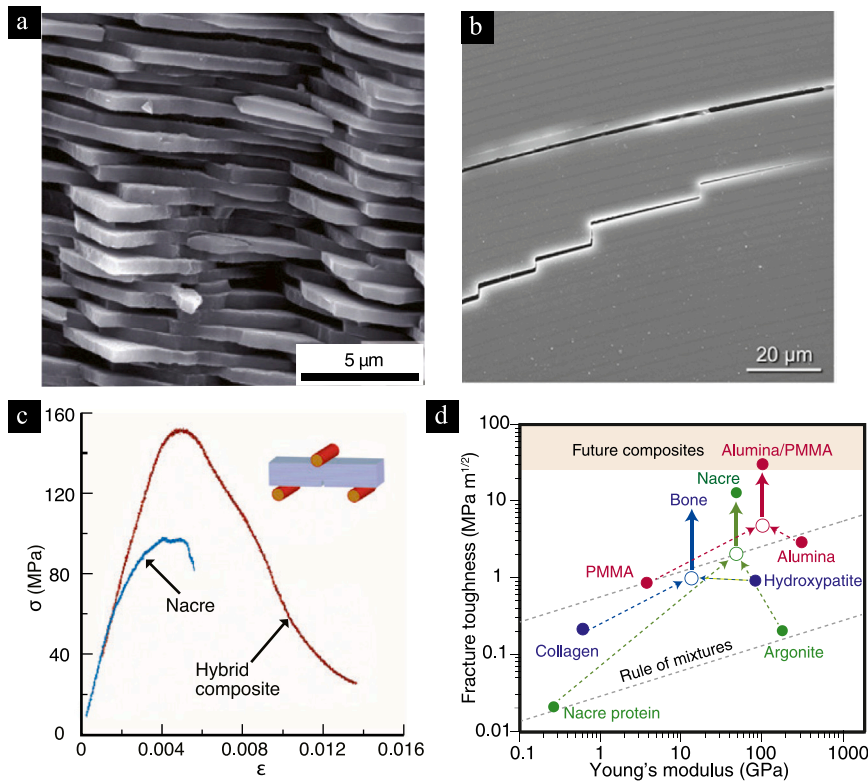


**Fig. 1.** (a) SEM micrograph of nacre showing the brick-and-mortar micro-architecture. Figure reproduced from Ritchie (2011). (b) SEM micrograph of *Monorhaphis chuni* (*M.chuni*) specimen subjected to a three point bend test. It is observed that the specimen before failure develops convoluted crack patterns due to crack deflection and arrest at the interfaces. Figure reproduced from Weaver et al. (2010). (c) A comparison of the stress–strain response obtained by edge notched three point bend testing of nacre and a synthetic composite made of 85 vol.% alumina indicates that the composite has both higher strength and toughness as compared to nacre. Figure reproduced from Ritchie (2011). (d) A summary of fracture toughness properties of structural biomaterials, hybrid composites in comparison to their respective constituents. Figure reproduced from Wegst et al. (2015).

fracture toughness is defined using the  $J$ -integral, which is computed using the outermost boundary of the domain as the contour of integration. Importantly, the length scales within the considered heterogeneous media were all comparable. In contrast, in SBs such as nacre, the compliant interfaces are orders of magnitude thinner than the stiff bricks.

The core challenge for any potential numerical method to simulate crack evolution in SBs is capturing the complex crack morphologies that have been demonstrated in experiments. Methods which represent the crack via sharp surfaces (or curves in 2D) face some difficulties with this task (Shen et al., 2017; Wan et al., 2019). Methods like the eXtended Finite Element Method (XFEM) (Moës et al., 1999, 2002; Sukumar et al., 2015) require an explicit representation of the crack geometry (such as a surface parameterization or a level set) to define enrichment functions. Crack growth is typically modeled via crack front (or crack tip in 2D) dynamics, for example with Griffith's criterion (Griffith, 1921); additional criteria or models are needed to incorporate crack branching and crack nucleation. Another class of sharp crack methods are based on cohesive zone models, such as Xu and Needleman (1994), Camacho and Ortiz (1996). In these methods, cohesive zone separation laws are imposed on the faces (or edges in 2D) between neighboring finite elements. This provides a unified framework for crack growth, crack nucleation, and crack branching, because cracks may nucleate and grow between any elements. However, this method is limited as the crack patterns are heavily mesh-dependent.

A family of models which can simulate complex crack morphologies uses phase fields to model fracture. With origins in continuum damage theory (Peerlings et al., 1996), phase transformation theory (Karma et al., 2001), and variational fracture theory (VFT) (Francfort and Marigo, 1998; Bourdin et al., 2000, 2008), these models replace sharp cracks with a diffuse damage field, the evolution of which models crack growth. In the case of RVFT, the damage field (i.e. the cracks) evolves such that the total energy (elastic plus fracture) of the system is minimized. Furthermore, the notion of  $\Gamma$ -convergence (Ambrosio and Tortorelli, 1990) provides a rigorous mathematical connection between the phase-field approximations of RVFT (Bourdin et al., 2000) and the original sharp-crack theory (Francfort and Larsen, 2003). Unlike sharp crack approaches, there are minimal prior restrictions on the distribution of damage in the problem domain, which means that a wide variety of crack morphologies may be simulated without mesh dependence, including crack branching and crack jumps across heterogeneities (Miehe et al., 2010b; Borden et al., 2012; Hossain et al., 2014). While RVFT and phase field models present their own difficulties, for example requiring large amounts

of mesh refinement to adequately resolve the damage field, their ability to produce realistic and complex crack morphologies is why we have chosen them as the basis of our approach for SBs.

Phase field models have been introduced to simulate fracture in the presence of weak interfaces. In Hansen-Dörr et al. (2019, 2020), the interface, which is nominally a surface of co-dimension 1 embedded within the bulk material, is replaced by a region with finite thickness. Within this region of finite thickness, the fracture toughness and/or elastic moduli are allowed to vary. In Hansen-Dörr et al. (2019), the fracture toughness is assigned a constant value within the wide interface; in Hansen-Dörr et al. (2020), the authors also explore smoother fracture toughness distributions and elastic moduli distributions. For the case of constant wide-interface fracture toughness, the authors derive relationships for the effective interface fracture toughness as a function of the bulk toughness, the assigned wide-interface fracture toughness, the wide-interface thickness, and the damage field length scale. These formulas are assessed numerically through examples.

Approaches taken after (Hansen-Dörr et al., 2019, 2020) generally follow a similar approach. For example, in Yoshioka et al. (2021), the authors adopt the approach of a constant fracture toughness within the wide interface as in Hansen-Dörr et al. (2019). In Zhou et al. (2022), the authors also assign constant fracture toughness within the wide interface; however, they also explore the case where the bulk fracture toughness is different on either side of the interface. Meanwhile, in Unnikrishna Pillai et al. (2023), a Gaussian kernel is used to create a smooth variation in the fracture toughness.

In this work, we modify the traditional regularization process for VFT (recapitulated in Sections 3.1 and 3.2) to incorporate materials whose fracture toughness may differ along interfaces with zero thickness. Such cases are representative of atomically-thin bonding in adhesive contact, grain boundaries in polycrystalline materials, or interfaces whose thickness is much smaller than other relevant problem dimensions (e.g., the organic phase in SBs). In our regularization approach, the interfaces are assigned finite (small) width, inside which the material has fracture toughness  $g_i$ , while the surrounding material has fracture toughness  $g_b$ . The interface width is chosen to scale proportionally with the fracture regularization length  $\epsilon$ , and is discussed further in Section 3.3. Under suitable assumptions, we prove the  $\Gamma$ -convergence result for arbitrary two-dimensional specimens in Section 4. A consequence of this result is that we quantify the effective interface fracture toughness  $g_{\text{int}}$  of the zero-thickness interface, which depends  $g_b$ ,  $g_i$ , and the proportionality constant of the interface width to  $\epsilon$ . Returning to the problem of crack evolution in SBs, we implement our modified regularization procedure within a phase-field model for irreversible, brittle fracture, see Section 5. In Section 6, we verify that the modified RVFT for interfaces (RVFTI) reproduces fracture toughness consistent with  $g_{\text{int}}$ , and we explore crack kinking at a bi-material interface. We then use RVFTI to study toughening mechanisms in SB-inspired configurations in Section 7. Lastly, we discuss the main results and conclude this work in Section 8.

We remark that our approach resembles the work of Hansen-Dörr et al. (2019, 2020) in that we replace an infinitesimally-thin interface by one with finite thickness and assign a constant fracture toughness  $g_i$  (that is different from  $g_{\text{int}}$ ) within. However, our approach is motivated by  $\Gamma$ -convergence; that is, we introduce a regularization to the variational fracture problem in a material with weak interfaces and we prove under some mild assumptions that the regularization  $\Gamma$ -converges to the original problem.

While the results in this work are particularized to two dimensional problems, we believe that the theory also applies in 3D. Three dimensional RVFTI simulations have been performed, but we do not present these here.

## 2. Mathematical preliminaries

### 2.1. Notation

We let unbolded symbols such as  $x$  and  $u$  denote scalars or scalar-valued fields, while we let bold symbols such as  $\mathbf{x}$  and  $\mathbf{u}$  denote vectors or vector-valued fields in  $\mathbb{R}^n$ . We denote sequences with parentheses:  $(a_n)_n := (a_1, a_2, a_3, \dots)$ . Depending on context,  $|\cdot|$  may indicate the absolute value of a scalar, the Euclidean norm of a vector, or the Frobenius norm of a tensor.

There are two important measures used in this manuscript. Further details on measure theory may be found in textbooks such as Evans and Gariepy (2015). For any subset  $A \subseteq \mathbb{R}^n$ , we let  $\mathcal{L}^n(A)$  denote the  $n$ -dimensional Lebesgue measure of  $A$  (which may be infinite). Integration with respect to this measure is written with the standard notation  $\int dx$ . Next, for  $A \subseteq \mathbb{R}^n$ , we let  $\mathcal{H}^m(A)$  denote the  $m$ -dimensional Hausdorff measure of  $A$  (where  $m$  may differ from  $n$ ), which is defined in two steps. First, for any  $\delta > 0$ ,

$$\mathcal{H}_\delta^m(A) = \inf \left\{ \alpha_m \sum_{i=1}^{\infty} \text{diam}(U_i)^m : A \subseteq \bigcup_{i=1}^{\infty} U_i, \text{diam}(U_i) < \delta \right\}, \quad (1a)$$

where  $\text{diam}(U) = \sup_{x,y \in U} |x - y|$  for any  $U \subseteq \mathbb{R}^n$ . Second, we take

$$\mathcal{H}^m(A) = \lim_{\delta \rightarrow 0} \mathcal{H}_\delta^m(A) = \sup_{\delta > 0} \mathcal{H}_\delta^m(A). \quad (1b)$$

As in Evans and Gariepy (2015, Definition 2.1), we define  $\mathcal{H}^m$  with a scaling constant  $\alpha_m$  so that  $\mathcal{H}^1$  coincides with the usual definition of arc length ( $\alpha_1 = 1$ ),  $\mathcal{H}^2$  coincides with the usual definition of surface area, etc. Integration with respect to the Hausdorff measure is written with the notation  $\int d\mathcal{H}^m(\mathbf{x})$ .

For any  $A \subseteq \mathbb{R}^n$ , we define  $\text{dist}(\cdot, A) : \mathbb{R}^n \rightarrow \mathbb{R}$  as the distance function to  $A$ . That is, for any  $\mathbf{x} \in \mathbb{R}^n$ ,

$$\text{dist}(\mathbf{x}, A) = \inf_{z \in A} |\mathbf{x} - z|.$$

We let  $\mathcal{N}_\rho(A) \subset \mathbb{R}^n$  denote the  $\rho$ -neighborhood of  $A$ , or

$$\mathcal{N}_\rho(A) = \{ \mathbf{x} \in \mathbb{R}^n : \text{dist}(\mathbf{x}, A) < \rho \}.$$

Let  $\mathcal{B}$  be an open subset of  $\mathbb{R}^n$ . For non-negative integer  $k$ , we let  $C^k(\mathcal{B}; \mathbb{R}^m)$  denote the space of functions  $f : \mathcal{B} \rightarrow \mathbb{R}^m$  whose derivatives up to order  $k$  are continuous. The space  $C^\infty(\mathcal{B}; \mathbb{R}^m)$  contains the functions with all derivatives continuous, while  $C_c^\infty(\mathcal{B}; \mathbb{R}^m) \subset C^\infty(\mathcal{B}; \mathbb{R}^m)$  are those functions which are compactly supported in  $\mathcal{B}$ . We let  $L^2(\mathcal{B}; \mathbb{R}^m)$  denote the space of functions for which  $\int_{\mathcal{B}} |f|^2 dx < \infty$  and  $H^1(\mathcal{B}; \mathbb{R}^m) \subset L^2(\mathcal{B}; \mathbb{R}^m)$  be the space of functions for which  $\int_{\mathcal{B}} |\nabla f|^2 dx < \infty$ , where the derivative is defined in the distributional sense. Finally, let  $L^\infty(\mathcal{B}; \mathbb{R}^m)$  be the space of functions which have finite essential supremum (roughly, which are bounded),  $\text{ess sup}_{x \in \mathcal{B}} |f(x)| < \infty$ . The usual norms on these spaces are denoted by  $\|\cdot\|_{L^2(\mathcal{B}; \mathbb{R}^m)}$ ,  $\|\cdot\|_{H^1(\mathcal{B}; \mathbb{R}^m)}$ , and  $\|\cdot\|_{L^\infty(\mathcal{B}; \mathbb{R}^m)}$ , respectively.

When referring to functions of time and space, e.g.  $f(t, \mathbf{x})$ , we will use the notation  $f(t)$  in place of  $f(t, \cdot)$  to refer to the function evaluated at time  $t$ .

### 3. Theory

#### 3.1. Variational principle of fracture

The concept of fracture toughness in elastic, brittle materials stems from the seminal work of Griffith (1921). Griffith postulated that there was an energy cost to the creation of new crack surfaces, proportional to the new surface area, and that this cost must be paid by releasing stored elastic energy in the body. With respect to an infinitesimal extension of a crack, Griffith’s criterion states that the stored energy release rate must be equal to a material constant. This notion implies a balance of energy during crack growth.

In Griffith’s original work, the material constant is twice the surface free energy of the bulk material, as the insertion of a crack creates two free surfaces which are assumed to perfectly coincide in the undeformed configuration.<sup>3</sup> In this work, we will refer to Griffith’s material constant as the “fracture toughness”, accounting for the crack surface as a single surface instead of two identical crack faces.<sup>4</sup>

Francfort and Marigo (1998) introduced variational fracture theory (VFT) as an extension of Griffith’s theory. Rather than considering the energetics of a single crack tip, a key postulate of VFT is that the solid deforms and cracks to (globally) minimize the total free energy, which is comprised of two parts: (i) the energy corresponding to elastic deformation and the work of applied external forces; and (ii) the energy needed to produce the crack surfaces. Respectively, we call these the “elastic energy” and “surface energy”. The relaxed conditions on the admissible cracks naturally allow for crack nucleation and the formation of other complex morphologies (such as crack branching, merging, etc.) to be captured.

Mathematically, the variational principle is stated as follows, see Fig. 2(a.i). We consider an elastic domain  $\mathcal{B} \subset \mathbb{R}^n$  which is subjected to applied displacements  $\hat{u}$  on a portion of the boundary  $\partial\mathcal{B}_u \subseteq \partial\mathcal{B}$ . Then, the crack set  $\Gamma$  and displacement field  $\mathbf{u}$  minimize the energy

$$\Pi(\mathbf{u}, \Gamma) = \int_{\mathcal{B} \setminus \Gamma} W(\mathbf{x}, \epsilon(\mathbf{u})) dx + g\mathcal{H}^{n-1}(\Gamma), \tag{2}$$

where  $W(\mathbf{x}, \epsilon) \geq 0$  is the strain energy density,  $\epsilon(\mathbf{u}) := (\nabla\mathbf{u} + \nabla\mathbf{u}^T)/2$  is the symmetrized displacement gradient (i.e., small-strain tensor), and  $g > 0$  is the fracture toughness.

For simplicity, we assume an isotropic, linear elastic constitutive response

$$W(\mathbf{x}, \epsilon) = \frac{1}{2} \lambda(\mathbf{x}) \text{tr}[\epsilon]^2 + \mu(\mathbf{x}) |\epsilon|^2, \tag{3}$$

where  $\text{tr}[\cdot]$  is the trace of a tensor and  $|\cdot|$  is the Frobenius norm of a tensor. The coefficients  $\lambda$  and  $\mu$  are the Lamé parameters, but we may also discuss the elastic behavior in terms of Young’s modulus  $E$  and Poisson’s ratio  $\nu$ . We allow these (strictly positive) coefficients to vary spatially to include situations like a crack along a bi-material interface, see Section 6.2.

An important question in the minimization of (2) is what are the admissible spaces for  $\mathbf{u}$  and  $\Gamma$ . The rigorous answer to this question is that  $\mathbf{u}$  should belong to the space of generalized special functions of bounded deformation,  $GSBD(\mathcal{B}; \mathbb{R}^n)$  (Ambrosio et al., 1997, 2000). Imprecisely, this space contains all functions whose symmetrized distributional derivative is a measure composed of two parts: the first is an integrable function (i.e.  $\epsilon(\mathbf{u})$ ) over  $\mathcal{B}$ , while the second corresponds to the jump in  $\mathbf{u}$  across its so-called jump set  $J_u$ . We immediately identify the crack set  $\Gamma$  with  $J_u$ . We refer the interested reader to Ambrosio et al. (1997, 2000) for further details.

Lastly, the global minimizers of (2) may not be physically or experimentally relevant. However, the computation of the global minimizers of (2) is a valuable exercise for the following two reasons.

<sup>3</sup> At smaller scales, this assumption may not be valid, as the surface roughness and fragmentation of material in between the crack faces can mean that the surface areas do not exactly coincide.

<sup>4</sup> Another common name for Griffith’s material constant is the “critical energy release rate”, while “fracture toughness” is also used for a critical value of the stress intensity factor around a crack tip. Since we do not refer to the critical stress intensity value in this work, we do not anticipate confusion in our terminology.

<sup>5</sup> We predominantly consider the  $n = 2$  case but will also briefly explore the  $n = 1$  case.

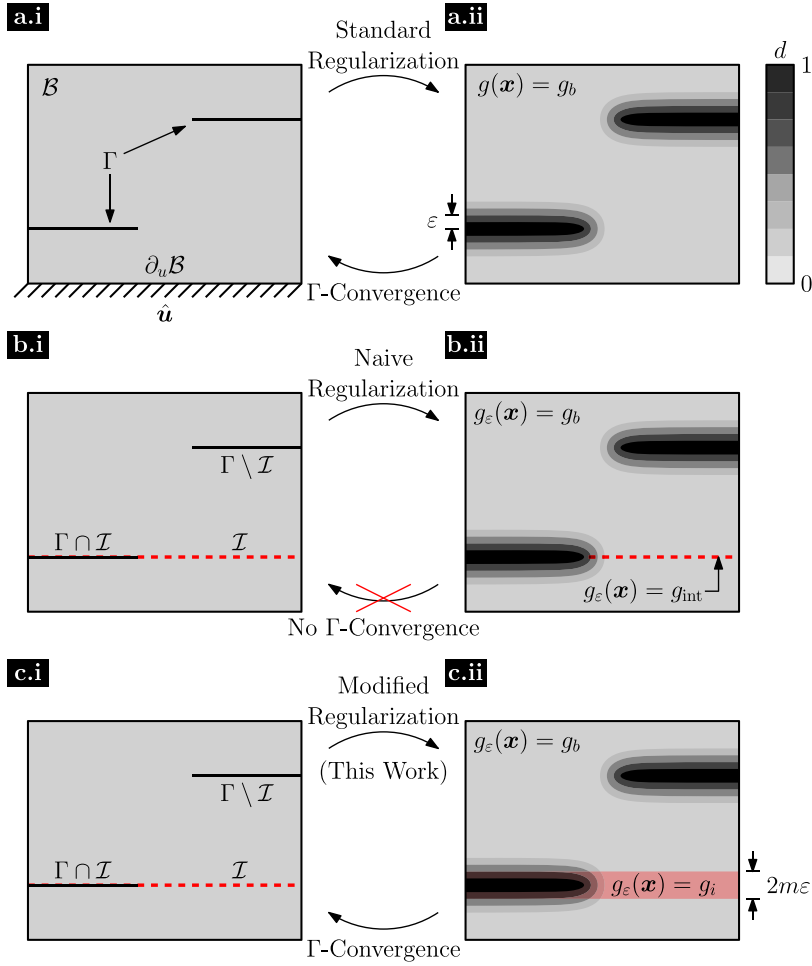


**Fig. 2.** Schematic representation of the interface fracture problem and its regularization. (a.i) Original variational fracture problem with no weak interfaces, crack set  $\Gamma$ , and applied Dirichlet boundary conditions. (a.ii) Standard regularization approach for the problem in (a.i), which replaces the crack set by a continuous damage field  $d$  taking value between 0 and 1. The damage field has characteristic length scale  $\epsilon$ . The standard regularization  $\Gamma$ -converges to the original problem as  $\epsilon \rightarrow 0$ . (b.i) Variational fracture problem with a weak interface  $\mathcal{I}$ . (b.ii) Naive approach to regularize the problem in (b.i) using standard regularization practices. The regularized problem has the same fracture toughness distribution  $g(x)$  as that of the original problem. Because the weak interface has zero measure, it is invisible to the damage field, and hence we do not recover the original problem as  $\epsilon \rightarrow 0$ . (c.i) Variational fracture problem with weak interface  $\mathcal{I}$ . (c.ii) The modified regularization approach proposed in this work. We modify the fracture toughness distribution by widening the weak interface by a factor of  $2m\epsilon$ , and we assign a fracture toughness  $g_i$  therein.

1. As mentioned in [Francfort and Marigo \(1998\)](#), local minimizers of the energy may be more experimentally relevant. However, there are cases where the local and global minimizers coincide. For example, in a double cantilever beam (DCB) specimen subjected to displacement-controlled loading, the elastic energy scales inversely with the cube of the crack length while the fracture energy grows linearly with crack length. The result is that the total energy is convex with respect to crack length, possessing a unique minimizer.
2. Numerical procedures aimed at solving the global minimization problem often follow a sequence of configurations that locally minimize, which can also provide some insights into the fracture process.

### 3.2. Regularization of the total energy

It is difficult to compute the minimizers of (2) because of the presence of both volumetric and surface energies. Borrowing from the ideas of image segmentation, [Bourdin et al. \(2000\)](#) introduced the following regularization, see [Fig. 2\(a.ii\)](#). We define a scalar-valued function  $d$  and a length scale  $\epsilon$ . We then seek minimizers  $(u, d)$  of the regularized energy

$$\Pi_\epsilon(u, d) = \int_B ((1 - d)^2 + k_\epsilon) W(x, \epsilon(u)) dx + \int_B \frac{g}{2} \left( \frac{d^2}{\epsilon} + \epsilon |\nabla d|^2 \right) dx \tag{4}$$

over the admissible spaces  $\mathcal{U}_u = \{v \in H^1(B; \mathbb{R}^n) : v \equiv \hat{u} \text{ on } \partial B_u\}$  and  $\mathcal{U}_d = H^1(B; \mathbb{R})$ . In the previous equation,  $k_\epsilon > 0$  is a parameter which is small compared with  $\epsilon$ .

We first note that the optimal  $d$  must take value between 0 and 1. These limits may be interpreted as pristine and fully-damaged material, respectively. Second, it has been shown (see Chambolle, 2005; Ambrosio and Tortorelli, 1992; Bourdin et al., 2008) that  $\Pi$  is the  $\Gamma$ -limit of  $\Pi_\epsilon$  as  $\epsilon \rightarrow 0$ . Consequently, the global minimizers of  $\Pi_\epsilon$  converge to those of  $\Pi$ , which provides a rational approach to approximate the minimizers of  $\Pi$ .

### 3.3. Regularization with interfaces

In (2) and (4), we assumed a constant fracture toughness  $g$  throughout the domain. However, it is possible to have spatial variation in fracture toughness throughout  $B$ . In particular, suppose there exists a weak interface  $I \subset B$ , which we assume to be a simple, rectifiable curve (or finite collection of curves) with fracture toughness  $g_{\text{int}}$ . Meanwhile, we suppose the remainder of the domain  $B \setminus I$  has uniform fracture toughness  $g_b > g_{\text{int}}$ . Under the original variational principle, cracks may form along this interface, and the surface energy will be less than if the same crack formed elsewhere in the domain. For this fracture toughness distribution, the total energy is

$$\Pi(u, \Gamma) = \int_{B \setminus \Gamma} W(x, \epsilon(u)) dx + g_b \mathcal{H}^{n-1}(\Gamma \setminus I) + g_{\text{int}} \mathcal{H}^{n-1}(\Gamma \cap I). \tag{5}$$

In the previous equation, another way to write the surface energy terms is

$$\int_{\Gamma} g(x) d\mathcal{H}^{n-1}(x), \tag{6a}$$

where

$$g(x) = \begin{cases} g_{\text{int}} & x \in I, \\ g_b & \text{otherwise.} \end{cases} \tag{6b}$$

Following the relationship between (2) and (4), and considering the expression for the surface energy in (6), we propose the following regularization of (5):

$$\Pi_\epsilon(u, d) = \int_B ((1-d)^2 + k_\epsilon) W(x, \epsilon(u)) dx + \int_B \frac{g_\epsilon(x)}{2} \left( \frac{d^2}{\epsilon} + \epsilon |\nabla d|^2 \right) dx. \tag{7a}$$

We are now faced with the question of what fracture toughness distribution  $g_\epsilon(x)$  we should use in order to recover (5) in the  $\Gamma$ -limit. Some options are as follows:

1. We can use the fracture toughness distribution (6b) for the sharp-crack problem (see Fig. 2(b)), i.e.

$$g_\epsilon(x) = g(x).$$

However, this approach faces a critical issue. Because  $g(x) - g_b$  is nonzero only when  $x \in I$ , and  $\mathcal{L}^n(I) = 0$ , then the second integral in (7a) is equal to that in (4). In other words, the damage field does not see the weak interface. Consequently, if we take the  $\Gamma$ -limit of  $\Pi_\epsilon$ , the limiting  $\Pi$  will not have reduced fracture toughness at the interface.

2. In order for the damage field to be influenced by the weak interface, we must make the weak interface occupy a set with finite measure. For example, we can widen the weak interfaces by some thickness  $2t > 0$ :

$$g_\epsilon(x) = \begin{cases} g_{\text{int}} & \text{dist}(x, I) \leq t, \\ g_b & \text{otherwise,} \end{cases}$$

where  $\text{dist}(x, I)$  is the distance between  $x$  and the interfaces  $I$ . This approach yields fracture toughness heterogeneities akin to those explored in Hossain et al. (2014). However, this approach no longer models a weak interface with negligible thickness. Hence, when we take the  $\Gamma$ -limit of  $\Pi_\epsilon$ , we no longer recover (5).

3. In order to recover thin weak interfaces, we must have  $t$  shrink to zero along with  $\epsilon$ . Our approach is to set  $t = m\epsilon$ , where  $m > 0$ , see Fig. 2(c). We define

$$g_\epsilon(x) = \begin{cases} g_i & \text{dist}(x, I) \leq m\epsilon, \\ g_b & \text{otherwise,} \end{cases} \tag{7b}$$

where  $g_i$  is determined from  $g_b, g_{\text{int}}$ , and  $m$  using:

$$g_i = \frac{\sqrt{(g_b - g_{\text{int}})^2 + 4g_b g_{\text{int}} \tanh^2(m) - (g_b - g_{\text{int}})}}{2 \tanh(m)}. \tag{7c}$$

This equation for  $g_i$  may seem arbitrary; however, as we will prove in Section 4, setting  $g_i$  in this way allows us to precisely recover the desired interface fracture toughness  $g_{\text{int}}$ .

For our proposed formulation, we remark that if we start with a regularized problem with widened interface  $g_i$  the limiting interface fracture toughness is given by

$$g_{\text{int}} = g_i \left( \frac{g_b + g_i \tanh(m)}{g_i + g_b \tanh(m)} \right), \quad (8)$$

which is the inverse of (7c). We observe from this formula that  $g_{\text{int}}$  varies monotonically from  $g_b$  when  $m = 0$  (zero-width interface) to  $g_i$  when  $m = \infty$  (the interface encapsulates the entire domain). Similarly, for a fixed  $m$ , (8) is a one-to-one function from  $g_i$  to  $g_{\text{int}} < g_b$ , meaning if we wish to model an interface with fracture toughness  $g_{\text{int}}$ , we can always find a suitable  $g_i$ .

#### 4. $\Gamma$ -Convergence proof for the interface toughness

In this section, we prove that the functional  $\Pi_\varepsilon$  defined in (7)  $\Gamma$ -converges to the functional  $\Pi$  in (5). Before formally stating and proving this result, we present some technical details. Readers who are more interested in numerics and simulation examples may skip this section and continue in Section 5.

##### 4.1. Technical details

We take the problem domain  $\mathcal{B} \subset \mathbb{R}^2$  to be bounded and to have Lipschitz boundary. Meanwhile, the interface set  $\mathcal{I} \subset \overline{\mathcal{B}}$  is assumed to be a finite union of rectifiable curves,  $(I_i)_i$ . Specifically, for each  $I_i$ , we assume that the arc-length parameterization  $\gamma_i : [0, \mathcal{H}^1(I_i)] \rightarrow \mathbb{R}^2$  is  $C^2$ -continuous and injective. Furthermore, for  $j \neq i$ , we request that  $I_i \cap I_j \subset \{\gamma_i(0), \gamma_i(\mathcal{H}^1(I_i))\}$ , with an identical condition holding for  $I_j \cap \partial\mathcal{B}$ . In other words, the individual curves comprising  $\mathcal{I}$  may only intersect each other at their endpoints and only the endpoints of  $I_i$  are allowed to touch the domain boundary  $\partial\mathcal{B}$ . For each  $s \in [0, \mathcal{H}^1(I_i)]$ , we set  $\hat{\boldsymbol{\gamma}}_i(s) = \boldsymbol{\gamma}'_i(s)$  to be the unit tangent vector at  $\boldsymbol{\gamma}_i(s)$ , and we define the unit normal at the same point,  $\hat{\boldsymbol{n}}_i(s)$ , through  $90^\circ$  rotation of  $\hat{\boldsymbol{\gamma}}_i(s)$ .<sup>6</sup> We sometimes abuse notation by writing  $\hat{\boldsymbol{\gamma}}_i(\boldsymbol{x})$  and  $\hat{\boldsymbol{n}}_i(\boldsymbol{x})$  for  $\boldsymbol{x} \in I_i$  instead of  $\hat{\boldsymbol{\gamma}}_i(\boldsymbol{\gamma}_i^{-1}(\boldsymbol{x}))$  and  $\hat{\boldsymbol{n}}_i(\boldsymbol{\gamma}_i^{-1}(\boldsymbol{x}))$ , respectively. For each curve, we may define the *signed* radius of curvature  $R_i$  as

$$\frac{1}{R_i(s)} = -\boldsymbol{\gamma}''_i(s) \cdot \hat{\boldsymbol{n}}_i(s). \quad (9)$$

Because of the regularity of the interface curves, there must exist a minimum radius of curvature over all  $s$  and over all curves,

$$R_{\min} = \min_i \min_{s \in [0, \mathcal{H}^1(I_i)]} |R_i(s)|. \quad (10)$$

Additionally, for each  $I_i$ , there exists  $\rho_i > 0$  such that the coordinate map

$$(s, z) \mapsto \boldsymbol{\gamma}_i(s) + z\hat{\boldsymbol{n}}_i(s) \quad (11)$$

on the domain  $[0, \mathcal{H}^1(I_i)] \times (-\rho_i, \rho_i)$  is a diffeomorphism (see Abate and Tovena (2012, Theorem 2.2.5)). The image of  $[0, \mathcal{H}^1(I_i)] \times (-\rho_i, \rho_i)$  under the map is called the tubular neighborhood of  $I_i$ . Moreover, it may be shown that  $\rho_i \leq \min_{s \in [0, \mathcal{H}^1(I_i)]} |R_i(s)|$ .

We next discuss the admissible function spaces for  $\Pi_\varepsilon$  and  $\Pi$ . For  $\Pi_\varepsilon$ , arguments  $(\boldsymbol{u}, d)$  belong to  $H^1(\mathcal{B}; \mathbb{R}^2) \times H^1(\mathcal{B}; \mathbb{R})$ . The functional  $\Pi$  is defined over the set

$$\mathcal{A} = \{ \boldsymbol{u} \in L^\infty(\mathcal{B}; \mathbb{R}^2) : \boldsymbol{u}|_{\mathcal{B} \setminus \Gamma} \in H^1(\mathcal{B} \setminus \Gamma; \mathbb{R}^2), \Gamma \in \mathcal{C} \}, \quad (12)$$

where  $\mathcal{C}$  is the set of all closed,  $\mathcal{H}^1$ -rectifiable subsets of  $\overline{\mathcal{B}}$ . Note that each  $\boldsymbol{u} \in \mathcal{A}$  has a corresponding  $\Gamma$  (the  $\Gamma$  is not defined separately). For  $\boldsymbol{u} \in \mathcal{A}$ , we also request that  $\boldsymbol{u}|_{\mathcal{B} \setminus \Gamma}$  be discontinuous across its corresponding  $\Gamma$ , except possibly at a countable number of points in  $\Gamma$ . In the parlance of  $SBD(\mathcal{B}; \mathbb{R}^2)$ , we say that  $\Gamma$  is the jump set of the function  $\boldsymbol{u}$ . We note that  $\mathcal{A}$  is slightly more restrictive than  $SBD(\mathcal{B}; \mathbb{R}^2)$ ; however, this space is suitable for the sorts of crack topologies that are expected in practical situations. We also remark that this set can be extended to functions whose crack set is not closed via the approximation results of Chambolle (2004, Theorem 3).

##### 4.2. Statement of the theorem

**Theorem 1.** *Let  $(\varepsilon_n)_n$  be a sequence of positive real numbers which converges to zero. Then the sequence of functionals  $(\Pi_{\varepsilon_n})_n$   $\Gamma$ -converges to  $\Pi$ . That is, for any  $\boldsymbol{u} \in \mathcal{A}$  (with corresponding set  $\Gamma$ ), the following hold.*

- i. ( $\Gamma$ -lim inf) For any sequences  $(\boldsymbol{u}_n)_n \subset H^1(\mathcal{B}; \mathbb{R}^2)$  and  $(d_n)_n \subset H^1(\mathcal{B}; \mathbb{R})$  such that  $\boldsymbol{u}_n \rightarrow \boldsymbol{u}$  in  $L^2(\mathcal{B}; \mathbb{R}^2)$ , we have

$$\liminf_{n \rightarrow \infty} \Pi_{\varepsilon_n}[\boldsymbol{u}_n, d_n] \geq \Pi[\boldsymbol{u}, \Gamma]. \quad (13)$$

- ii. ( $\Gamma$ -lim sup) There exists sequences  $(\boldsymbol{u}_n)_n \subset H^1(\mathcal{B}; \mathbb{R}^2)$  and  $(d_n)_n \subset H^1(\mathcal{B}; \mathbb{R})$  such that  $\boldsymbol{u}_n \rightarrow \boldsymbol{u}$  in  $L^2(\mathcal{B}; \mathbb{R}^2)$  and

$$\limsup_{n \rightarrow \infty} \Pi_{\varepsilon_n}[\boldsymbol{u}_n, d_n] \leq \Pi[\boldsymbol{u}, \Gamma]. \quad (14)$$

In the following sections, we separately prove each of the two items in the above theorem.

<sup>6</sup> More precisely, we may find an orthogonal transformation  $\boldsymbol{Q} : \mathbb{R}^2 \rightarrow \mathbb{R}^2$  such that  $\boldsymbol{v} \cdot (\boldsymbol{Q}\boldsymbol{v}) = 0$  for any  $\boldsymbol{v} \in \mathbb{R}^2$ . Then, we set  $\hat{\boldsymbol{n}}_i(s) = \boldsymbol{Q}\hat{\boldsymbol{\gamma}}_i(s)$  for each  $s \in [0, \mathcal{H}^1(I_i)]$  and for each  $i$ .



4.3. Proof of  $\Gamma$ -lim inf

Before we prove [Theorem 1\(i\)](#), we require some preliminary results. For brevity, we leave the proofs to the appendices.

The first result concerns the portions of the tubular neighborhood of each  $I_i$  which do not overlap with the tubular neighborhood belonging to another  $I_j$  or with  $\partial B$ .

**Proposition 2.** For any  $\rho > 0$ , let  $\ell_{ix\rho}$  be the segment of length  $2\rho$ , centered at point  $x \in I_i$  and orthogonal to  $I_i$ , i.e.,

$$\ell_{ix\rho} = \{x + z\hat{n}_i(x) : z \in (-\rho, \rho)\}.$$

For each  $i$ , define  $J_i = \partial B \cup \left(\bigcup_{j \neq i} I_j\right) \cup \{\gamma_i(0), \gamma_i(H^1(I_i))\}$ . Then, for

$$0 < \rho < \min_i \left\{ \min \left\{ \rho_i, \max_{0 \leq s \leq H^1(I_i)} \frac{\text{dist}(\gamma_i(s), J_i)}{3} \right\} \right\}$$

the sets  $(A_{i\rho})_i$  with

$$A_{i\rho} := \gamma_i(\{s \in [0, H^1(I_i)] : \text{dist}(\gamma_i(s), J_i) > 3\rho\})$$

are nonempty and have the following properties.

1. For any  $x \in A_{i\rho}$ ,  $\ell_{ix\rho} \cap \ell_{jy\rho} = \emptyset$  for any  $y \in I_j$  (including the case where  $j = i$  and  $y \neq x$ ) and  $\ell_{ix\rho} \cap \partial B = \emptyset$ .
2. For any  $x \in A_{i\rho}$  and  $y \in \ell_{ix\rho}$ ,  $\text{dist}(y, I) = \text{dist}(y, I_i) = |y - x|$ .
3. As  $\rho$  decreases to 0,

$$\lim_{\rho \rightarrow 0^+} \mathcal{H}^1(I_i \setminus A_{i\rho}) = 0,$$

so that

$$\lim_{\rho \rightarrow 0^+} \mathcal{H}^1(\Gamma \cap A_{i\rho}) = \mathcal{H}^1(\Gamma \cap I_i).$$

The second result is a specialized  $\Gamma$ -lim inf result for the one-dimensional domain  $B = (-\rho, \rho)$  containing a crack at  $z = 0$ .

**Proposition 3** (One-dimensional  $\Gamma$ -lim inf). Suppose  $u \in L^2((-\rho, \rho); \mathbb{R})$ , but  $u|_{(-\delta, \delta)} \notin H^1((-\delta, \delta); \mathbb{R})$  for any  $0 < \delta \leq \rho$ . Let  $(u_n)_n, (d_n)_n \subset H^1((-\rho, \rho); \mathbb{R})$  be such that  $u_n \rightarrow u$  in  $L^2((-\rho, \rho); \mathbb{R})$ . Then, for any constant  $C > 0$ ,

$$\liminf_{n \rightarrow \infty} \left[ \int_{-\rho}^{\rho} (1 - d_n)^2 C (u'_n)^2 \, dz + \int_{-\rho}^{\rho} \frac{\bar{g}(z/\varepsilon_n)}{2} \left( \frac{d_n^2}{\varepsilon_n} + \varepsilon_n (d'_n)^2 \right) \, dz \right] \geq g_{\text{int}}, \tag{15a}$$

where

$$\bar{g}(t) := \begin{cases} g_i & \text{if } |t| \leq m, \\ g_b & \text{otherwise.} \end{cases} \tag{15b}$$

We remark that in our formulation [\(7b\)](#),  $g_\varepsilon(x) = \bar{g}(\text{dist}(x, I)/\varepsilon)$ . With these results, we are now ready for the proof.

**Proof of [Theorem 1\(i\)](#).**

1. Without loss of generality, assume that the sequences  $(u_n, d_n)_n$  are such that

$$\liminf_{n \rightarrow \infty} \Pi_{\varepsilon_n}[u_n, d_n] < \infty.$$

Otherwise, it is trivial to bound the limit inferior from below by any finite value we choose. Also, without loss of generality, we may assume that  $(\varepsilon_n)_n$  is a strictly decreasing sequence.

2. Fix  $\rho > 0$  (which will be specified later) and consider the  $\rho$ -neighborhood of  $I$ . We partition the domain into  $B \setminus \mathcal{N}_\rho(I)$  and  $\mathcal{N}_\rho(I) \cap B$ , and we apply superadditivity of the limit inferior:

$$\liminf_{n \rightarrow \infty} \Pi_{\varepsilon_n}[u_n, d_n] \geq \liminf_{n \rightarrow \infty} \Pi_{\varepsilon_n}[u_n, d_n, B \setminus \mathcal{N}_\rho(I)] + \liminf_{n \rightarrow \infty} \Pi_{\varepsilon_n}[u_n, d_n, \mathcal{N}_\rho(I) \cap B], \tag{16}$$

where for a subset  $\Omega \subset B$  we define  $\Pi_\varepsilon[\cdot, \cdot, \Omega]$  to be the same as in [\(7a\)](#), but integrated over  $\Omega$  instead of  $B$ . As  $\varepsilon_n \rightarrow 0$ , we will eventually have  $m\varepsilon_n < \rho$ , so that  $\mathcal{N}_{m\varepsilon_n}(I) \subset \mathcal{N}_\rho(I)$ . Going forward, we assume  $n$  is sufficiently large so that this is the case.

3. We consider separately each of the two terms on the right-hand-side of [\(16\)](#). For the first term, since we have cut out the widened interfaces,  $g_\varepsilon(x) \equiv g_b$  in  $B \setminus \mathcal{N}_\rho(I)$ . In this domain, we may apply standard  $\Gamma$ -convergence results such as [Chambolle \(2004, Theorem 4\)](#):

$$\liminf_{n \rightarrow \infty} \Pi_{\varepsilon_n}[u_n, d_n, B \setminus \mathcal{N}_\rho(I)] \geq \int_{B \setminus (\Gamma \cup \mathcal{N}_\rho(I))} W(x, \varepsilon(u)) \, dx + g_b \mathcal{H}^1(\Gamma \setminus \mathcal{N}_\rho(I)).$$

4. For the second term of (16), let us choose a subsequence  $(\mathbf{u}_{n_k}, d_{n_k})_k$  of  $(\mathbf{u}_n, d_n)_n$  for which.

$$\lim_{k \rightarrow \infty} \Pi_{\varepsilon_{n_k}}[\mathbf{u}_{n_k}, d_{n_k}, \mathcal{N}_\rho(I) \cap B] = \liminf_{n \rightarrow \infty} \Pi_{\varepsilon_n}[\mathbf{u}_n, d_n, \mathcal{N}_\rho(I) \cap B].$$

Going forward, we will abuse notation by referring to the subsequence as  $(\mathbf{u}_n, d_n)_n$ . Next, apply Proposition 2 to construct the sets  $A_{i\rho}$ . We recall that each set  $A_{i\rho}$  contains all points  $\mathbf{x} \in I_i$  such that the orthogonal segment  $\ell_{ix\rho} := \{\mathbf{x} + z\hat{\mathbf{n}}_i(\mathbf{x}) : z \in (-\rho, \rho)\}$  does not intersect  $\partial B$  or any other orthogonal segment  $\ell_{jy\rho}$  with  $\mathbf{y} \in I_j$  (which includes  $\mathbf{y} \in I_i$ ). Let  $\mathcal{T}_{i\rho} = \{\ell_{ix\rho} : \mathbf{x} \in \Gamma \cap A_{i\rho}\} \subset \mathcal{N}_\rho(I) \cap B$ . We assume that  $\rho < R_{\min}$  is sufficiently small enough that each  $A_{i\rho}$  (and hence  $\mathcal{T}_{i\rho}$ ) is not empty. By construction,  $\mathcal{T}_{i\rho} \cap \mathcal{T}_{j\rho} = \emptyset$  when  $i \neq j$ . Then, we trivially have

$$\Pi_{\varepsilon_n}[\mathbf{u}_n, d_n, \mathcal{N}_\rho(I) \cap B] \geq \Pi_{\varepsilon_n}[\mathbf{u}_n, d_n, (\cup_i \mathcal{T}_{i\rho})] = \sum_i \Pi_{\varepsilon_n}[\mathbf{u}_n, d_n, \mathcal{T}_{i\rho}].$$

5. We briefly discuss integration within each  $\mathcal{T}_{i\rho}$ . We use the coordinate map (11) defined for  $(s, z) \in [0, \mathcal{H}^1(I_i)] \times (-\rho, \rho)$ , which has Jacobian

$$1 + \frac{z}{R_i(s)} \geq 1 - \frac{\rho}{R_{\min}} > 0,$$

where the first inequality is a consequence of (10) and the second inequality is because  $\rho$  is chosen to be smaller than  $R_{\min}$ . Then, for any integrand  $f(\mathbf{x})$ , going to coordinates gives

$$\int_{\mathcal{T}_{i\rho}} f(\mathbf{x}) \, d\mathbf{x} = \int_{\gamma_i^{-1}(\Gamma \cap A_{i\rho})} \int_{-\rho}^{\rho} f(\mathbf{x}(s, z)) \left(1 + \frac{z}{R_i(s)}\right) \, dz ds.$$

Using the lower bound on the Jacobian, we have

$$\int_{\mathcal{T}_{i\rho}} f(\mathbf{x}) \, d\mathbf{x} \geq \left(1 - \frac{\rho}{R_{\min}}\right) \int_{\gamma_i^{-1}(\Gamma \cap A_{i\rho})} \int_{-\rho}^{\rho} f(\mathbf{x}(s, z)) \, dz ds.$$

In this way, we have transformed an integral over  $\mathcal{T}_{i\rho}$  into an integral over the rectangles  $\gamma_i^{-1}(\Gamma \cap A_{i\rho}) \times (-\rho, \rho)$ .

6. As shorthand, let us denote the two functionals in (7a) as  $\Pi_\varepsilon^e$  and  $\Pi_\varepsilon^f$ , respectively, for the elastic and surface energy terms. We may extend the normal vector  $\hat{\mathbf{n}}_i$  away from  $I_i$  and into  $\mathcal{T}_{i\rho}$  through the coordinate map; abusing notation, we have  $\hat{\mathbf{n}}_i(\mathbf{x}(s, z)) = \hat{\mathbf{n}}_i(s)$ . Then, for  $\Pi_\varepsilon^e$  we trivially have

$$\Pi_{\varepsilon_n}^e[\mathbf{u}_n, d_n, \mathcal{T}_{i\rho}] \geq \int_{\mathcal{T}_{i\rho}} (1 - d_n)^2 C_{\lambda\mu} |\hat{\mathbf{n}}_i \cdot \nabla \mathbf{u}_n \cdot \hat{\mathbf{n}}_i|^2 \, d\mathbf{x},$$

where  $C_{\lambda\mu}$  is a constant depending on the elastic moduli such that  $W(\mathbf{x}, \boldsymbol{\varepsilon}(\mathbf{u})) \geq C_{\lambda\mu} |\boldsymbol{\varepsilon}(\mathbf{u})|^2$ .<sup>7</sup> In the above, we also used the fact that  $|\boldsymbol{\varepsilon}(\mathbf{u})| \geq |\mathbf{v} \cdot \nabla \mathbf{u} \cdot \mathbf{v}|$  for any unit vector  $\mathbf{v}$ .

7. Following Step 5, we go to coordinates. Let us define the scalar function  $u_{zn}(s, z) = \mathbf{u}_n(\mathbf{x}(s, z)) \cdot \hat{\mathbf{n}}_i(\mathbf{x}(s, z))$  and abuse notation by writing  $d_n(s, z) = d_n(\mathbf{x}(s, z))$ . Then,  $\partial u_{zn} / \partial z = \hat{\mathbf{n}}_i \cdot \nabla \mathbf{u}_n \cdot \hat{\mathbf{n}}_i$ , and so

$$\Pi_{\varepsilon_n}^e[\mathbf{u}_n, d_n, \mathcal{T}_{i\rho}] \geq \left(1 - \frac{\rho}{R_{\min}}\right) \int_{\gamma_i^{-1}(\Gamma \cap A_{i\rho})} \int_{-\rho}^{\rho} (1 - d_n)^2 C_{\lambda\mu} \left| \frac{\partial u_{zn}}{\partial z} \right|^2 \, dz ds.$$

8. Similarly, for  $\Pi_\varepsilon^f$ , we note that  $|\nabla d_n| \geq |\nabla d_n \cdot \hat{\mathbf{n}}_i| = |\partial d_n / \partial z|$ , and so

$$\Pi_{\varepsilon_n}^f[\mathbf{u}_n, d_n, \mathcal{T}_{i\rho}] \geq \left(1 - \frac{\rho}{R_{\min}}\right) \int_{\gamma_i^{-1}(\Gamma \cap A_{i\rho})} \int_{-\rho}^{\rho} \frac{\bar{g}(z/\varepsilon_n)}{2} \left( \frac{d_n^2}{\varepsilon_n} + \varepsilon_n \left| \frac{\partial d_n}{\partial z} \right|^2 \right) \, dz ds.$$

In the previous inequality, we used the fact that  $g_{\varepsilon_n}(\mathbf{x}) = \bar{g}(\text{dist}(\mathbf{x}, I)/\varepsilon_n)$ , where  $\bar{g}$  is defined in (15b), and  $\text{dist}(\mathbf{x}, I)$  is precisely  $z$  for points in  $\mathcal{T}_{i\rho}$  (see Proposition 2).

9. Let  $\Theta = \gamma_i^{-1}(\Gamma \cap A_{i\rho}) \times (-\rho, \rho)$  be the parametric domain for  $(s, r)$ . Then,  $u_{zn}, d_n \in H^1(\Theta; \mathbb{R})$  and  $u_z := \mathbf{u} \cdot \hat{\mathbf{n}}_i$  belongs to  $L^2(\Theta; \mathbb{R})$ . We now apply two slicing results. First, by the slicing property of  $H^1$  functions (see Evans and Gariepy (2015, Theorem 4.21)), for almost-every  $s \in \gamma_i^{-1}(\Gamma \cap A_{i\rho})$ , the restrictions of  $u_{zn}$  and  $d_n$ <sup>8</sup> to the segment  $\{s\} \times (-\rho, \rho)$ , which we call  $u_{zn}|_s$  and  $d_n|_s$ , respectively, belong to  $H^1((-\rho, \rho); \mathbb{R})$ ; moreover,  $(u_{zn}|_s)'$  and  $(d_n|_s)'$  coincide for almost every  $z \in (-\rho, \rho)$  with  $\partial u_{zn} / \partial z$  and  $\partial d_n / \partial z$ . Second, via Fubini's Theorem and Evans and Gariepy (2015, Theorem 1.21), there exists a subsequence  $(u_{zn_k}, d_{nk})_k$  of  $(u_{zn}, d_n)_n$  for which  $u_{zn_k}|_s$  converges in  $L^2((-\rho, \rho); \mathbb{R})$  to  $u_z|_s$  for almost every  $s \in \gamma_i^{-1}(\Gamma \cap A_{i\rho})$ . Moreover, because of the assumptions on  $\mathbf{u} \in \mathcal{A}$ , we know that  $u_z|_s$  must be discontinuous across the crack set, in particular  $z = 0$ . Finally, as before, we abuse notation and refer to the subsequence as  $(u_{zn}, d_n)_n$ .

<sup>7</sup> The constant  $C_{\lambda\mu}$  is precisely the minimum eigenvalue of the fourth-order elasticity tensor  $\mathbb{C}$ , which is defined so that (3) is equivalent to  $W(\mathbf{x}, \boldsymbol{\varepsilon}(\mathbf{u})) = \frac{1}{2} \boldsymbol{\varepsilon}(\mathbf{u}) : (\mathbb{C}(\mathbf{x}) : \boldsymbol{\varepsilon}(\mathbf{u}))$ .

<sup>8</sup> More precisely, there are representatives in the equivalence classes of  $u_{zn}$  and  $d_n$  for which this property holds; however, we abuse notation and do not distinguish between the representative and the equivalence class.

10. For almost every  $s \in \gamma_i^{-1}(\Gamma \cap A_{i\rho})$ , if we define

$$f_n(s) := \int_{-\rho}^{\rho} (1 - d_n|s|)^2 C_{\lambda\mu}((u_{zn}|s|)')^2 dz + \int_{-\rho}^{\rho} \frac{\bar{g}(z/\varepsilon_n)}{2} \left( \frac{(d_n|s|)^2}{\varepsilon_n} + \varepsilon_n((d_n|s|)')^2 \right) dz,$$

then by the one-dimensional  $\Gamma$ -liminf result, [Proposition 3](#), we have

$$\liminf_{n \rightarrow \infty} f_n(s) \geq g_{\text{int}}.$$

Applying Fatou's lemma (and the sub-additivity of the lim inf), we have

$$\begin{aligned} \liminf_{n \rightarrow \infty} \int_{\gamma_i^{-1}(\Gamma \cap A_{i\rho})} f_n(s) ds &\geq \int_{\gamma_i^{-1}(\Gamma \cap A_{i\rho})} \liminf_{n \rightarrow \infty} f_n(s) ds \\ &\geq \int_{\gamma_i^{-1}(\Gamma \cap A_{i\rho})} g_{\text{int}} ds \\ &= g_{\text{int}} \mathcal{H}^1(\Gamma \cap A_{i\rho}). \end{aligned}$$

11. By the choice of subsequences in [Steps 4](#) and [9](#), we have that

$$\liminf_{n \rightarrow \infty} \Pi_{\varepsilon_n} [u_n, d_n, \mathcal{N}_\rho(I) \cap B] \geq \left(1 - \frac{\rho}{R_{\min}}\right) g_{\text{int}} \sum_i \mathcal{H}^1(\Gamma \cap A_{i\rho}).$$

12. Finally, we put together the estimates for  $B \setminus \mathcal{N}_\rho(I)$  and  $\mathcal{N}_\rho(I) \cap B$ :

$$\liminf_{n \rightarrow \infty} \Pi_{\varepsilon_n} [u_n, d_n] \geq \int_{B \setminus (\Gamma \cup \mathcal{N}_\rho(I))} W(x, \varepsilon(u)) dx + g_b \mathcal{H}^1(\Gamma \setminus \mathcal{N}_\rho(I)) + \left(1 - \frac{\rho}{R_{\min}}\right) g_{\text{int}} \sum_i \mathcal{H}^1(\Gamma \cap A_{i\rho}).$$

Since the left-hand-side is independent of  $\rho$ , we may shrink  $\rho$  to zero. We proceed term by term:

- (a) The strain energy density  $W(\cdot, \varepsilon(u))$  belongs to  $L^1(B \setminus \Gamma; \mathbb{R})$  and is non-negative. Thus,  $\mathcal{L}^2 \llcorner W(\cdot, \varepsilon(u))$  is a measure on subsets of  $B \setminus \Gamma$  (cf. [Vol'pert and Hudjaev \(1985, §3.2\)](#)). Because

$$\bigcup_{\rho > 0} B \setminus (\Gamma \cup \mathcal{N}_\rho) = B \setminus (\Gamma \cup I),$$

by continuity of measures on nested sets, we have

$$\lim_{\rho \rightarrow 0+} \int_{B \setminus (\Gamma \cup \mathcal{N}_\rho(I))} W(x, \varepsilon(u)) dx = \int_{B \setminus (\Gamma \cup I)} W(x, \varepsilon(u)) dx = \int_{B \setminus \Gamma} W(x, \varepsilon(u)) dx.$$

For the last equality, we used the fact that any function  $f \in L^1(B \setminus (\Gamma \cup I); \mathbb{R})$  also belongs to  $L^1(B \setminus \Gamma; \mathbb{R})$ , since  $\mathcal{L}^2(I) = 0$  and we may arbitrarily define values for  $f$  along  $I$  without changing the integral.

- (b) Similarly, for the nesting sets  $(\Gamma \setminus \mathcal{N}_\rho(I))_\rho$ , continuity of the Hausdorff measure gives

$$\lim_{\rho \rightarrow 0+} \mathcal{H}^1(\Gamma \setminus \mathcal{N}_\rho(I)) = \mathcal{H}^1(\Gamma \setminus I).$$

- (c) Since  $R_{\min}$  is independent of  $\rho$ ,

$$\lim_{\rho \rightarrow 0+} \left(1 - \frac{\rho}{R_{\min}}\right) = 1.$$

- (d) Finally, by construction of  $A_{i\rho}$ , we have

$$\lim_{\rho \rightarrow 0+} \sum_i \mathcal{H}^1(\Gamma \cap A_{i\rho}) = \sum_i \mathcal{H}^1(\Gamma \cap I_i) = \mathcal{H}^1(\Gamma \cap I).$$

Hence

$$\liminf_{n \rightarrow \infty} \Pi_{\varepsilon_n} [u_n, d_n] \geq \int_{B \setminus \Gamma} W(x, \varepsilon(u)) dx + g_b \mathcal{H}^1(\Gamma \setminus I) + g_{\text{int}} \mathcal{H}^1(\Gamma \cap I).$$

as desired.  $\square$

#### 4.4. Proof of $\Gamma$ -lim sup

Next, we prove [Theorem 1\(ii\)](#). We require a preliminary result for this step, the proof of which is left to the appendices, which concerns the arc length of the boundary of the  $\rho$ -neighborhood of a  $C^2$  curve.

**Proposition 4.** For any  $I_i$ , let  $0 \leq s_1 < s_2 \leq \mathcal{H}^1(I_i)$ . Then, for  $\rho < R_{\min}$ ,

$$\mathcal{H}^1(\partial \mathcal{N}_\rho(\gamma_i([s_1, s_2]))) \leq 4\pi\rho + 2 \left(1 + \frac{\rho}{R_{\min}}\right) \mathcal{H}^1(\gamma_i([s_1, s_2]))$$

We are now ready for the proof. Throughout this proof, we make use of the  $\Gamma$ -convergence proof of Chambolle (2004, Theorem 4) for domains with constant fracture toughness.

**Proof of Theorem 1(ii).**

1. Without loss of generality, we assume that for each  $I_i$ , the set  $\Gamma \cap I_i$  may be decomposed into the images of  $J_i$  disjoint closed intervals contained in  $[0, \mathcal{H}^1(I_i)]$ ,  $(\gamma_i([s_{j1}, s_{j2}]))_{j=1}^{J_i}$ .<sup>9</sup> Let  $(\Gamma_j)_j$  be the collection of all the subsets over all  $I_i$ , and let  $J = \sum_j J_i$  be the total number of subsets. Because the subsets are disjoint for each  $I_i$ , while  $I_i$  and  $I_j$  may intersect only at their endpoints,  $\mathcal{H}^1(\Gamma \cap I) = \sum_j \mathcal{H}^1(\Gamma_j)$ .
2. Construct a sequence  $(\alpha_n)_n$  converging to 0 such that  $\alpha_n = o(\varepsilon_n)$ , ensuring  $k_{\varepsilon_n} = o(\alpha_n)$  as in Chambolle (2004, Theorem 4).
3. We now construct the recovery sequences  $(\mathbf{u}_n)_n$  and  $(d_n)_n$ . As in Chambolle (2004, Theorem 4), define

$$\mathbf{u}_n(\mathbf{x}) = \begin{cases} \mathbf{0} & \text{dist}(\mathbf{x}, \Gamma) < \alpha_n/2, \\ \left(\frac{2\text{dist}(\mathbf{x}, \Gamma)}{\alpha_n} - 1\right) \mathbf{u}(\mathbf{x}) & \alpha_n/2 \leq \text{dist}(\mathbf{x}, \Gamma) < \alpha_n, \\ \mathbf{u}(\mathbf{x}) & \text{otherwise.} \end{cases}$$

By the regularity of the distance function, it is straightforward to show that  $\mathbf{u}_n \in H^1(\mathcal{B}; \mathbb{R}^2)$  and  $\|\mathbf{u}_n - \mathbf{u}\|_{L^2(\mathcal{B}; \mathbb{R}^2)} \rightarrow 0$  as  $n \rightarrow \infty$ . Moreover, since  $|\mathbf{u}_n(\mathbf{x})| \leq |\mathbf{u}(\mathbf{x})|$  for almost every  $\mathbf{x} \in \mathcal{B}$ , we have  $\|\mathbf{u}_n\|_{L^\infty(\mathcal{B}; \mathbb{R}^2)} \leq \|\mathbf{u}\|_{L^\infty(\mathcal{B}; \mathbb{R}^2)}$ .

4. Next, let

$$\bar{d}_n(t) = \begin{cases} \exp\left(\frac{\alpha_n - |t|}{2\varepsilon_n}\right) & |t| \geq \alpha_n \\ 1 & |t| < \alpha_n. \end{cases}$$

We remark that the function  $\bar{d}_n(\text{dist}(\mathbf{x}, \Gamma \setminus I))$  is precisely that used in the recovery sequence by Chambolle. Here, we will use this function around the bulk (i.e., non-interfacial) cracks.

5. Around the interface cracks, we require another damage profile  $d$ . Let  $\rho > 0$  and define

$$\bar{d}_n(t) = \begin{cases} 0 & |t| \geq \rho, \\ \frac{2g_i \sinh\left(\frac{|t| - \rho}{\varepsilon_n}\right)}{(g_b + g_i) \sinh\left(\frac{\alpha_n - \rho}{\varepsilon_n}\right) + (g_i - g_b) \sinh\left(\frac{\alpha_n - 2m\varepsilon_n + \rho}{\varepsilon_n}\right)} & m\varepsilon_n \leq |t| < \rho, \\ \frac{(g_b + g_i) \sinh\left(\frac{|t| - \rho}{\varepsilon_n}\right) + (g_i - g_b) \sinh\left(\frac{|t| - 2m\varepsilon_n + \rho}{\varepsilon_n}\right)}{(g_b + g_i) \sinh\left(\frac{\alpha_n - \rho}{\varepsilon_n}\right) + (g_i - g_b) \sinh\left(\frac{\alpha_n - 2m\varepsilon_n + \rho}{\varepsilon_n}\right)} & \alpha_n \leq |t| < m\varepsilon_n, \\ 1 & |t| < \alpha_n. \end{cases}$$

In the prior equation, we have assumed that  $\alpha_n < m\varepsilon_n < \rho$ . Because  $\alpha_n = o(\varepsilon_n)$ , we can always choose  $n$  sufficiently large so that this is the case. The function  $\bar{d}_n(t)$  is computed by minimizing

$$\bar{\Pi}_{\varepsilon_n}^f[d] = \int_{-\rho}^{\rho} \frac{\bar{g}(t/\varepsilon_n)}{2} \left(\frac{d^2}{\varepsilon_n} + \varepsilon_n(d')^2\right) dt$$

over the set

$$\mathcal{V}_{\alpha_n \rho_n} := \{d \in H^1((-\rho, \rho); \mathbb{R}) : d(t) = 1 \text{ for } t \in [-\alpha_n, \alpha_n], d(\pm\rho) = 0\},$$

and extending the minimizer by 0 outside of the interval  $[-\rho, \rho]$  (compare with the proof of Proposition 3). By construction,

$$\lim_{n \rightarrow \infty} \bar{\Pi}_{\varepsilon_n}^f[\bar{d}_n] = g_{\text{int}}.$$

6. Finally, we build  $d_n$  as the point-wise maximum of  $\bar{d}_n$  and  $\bar{d}_n$ :

$$d_n(\mathbf{x}) = \max \left\{ \bar{d}_n(\text{dist}(\mathbf{x}, \Gamma \setminus \mathcal{N}_\rho(I))), \bar{d}_n(\text{dist}(\mathbf{x}, \Gamma \cap I)) \right\},$$

where  $\rho$  is chosen to be the same as in the previous step. Just like the constituent functions, we remark that  $0 \leq d_n \leq 1$ . Moreover,  $d_n(\mathbf{x}) = 1$  whenever  $\mathbf{x} \in \mathcal{N}_{\alpha_n}(\Gamma)$ . Importantly,  $d_n$  is Lipschitz continuous (as it is the point-wise maximum of the

<sup>9</sup> This assumption is not terribly restrictive, see Proposition 8. For any  $\eta > 0$ , we can cover  $\Gamma \cap I_i$  by  $N_{i\eta}$  pairwise disjoint, simply connected, closed subsets  $(A_j)_j$  so that

$$\mathcal{H}(\Gamma \cap I_i) \leq \sum_{j=1}^{N_{i\eta}} \mathcal{H}^1(A_j) \leq \mathcal{H}(\Gamma \cap I_i) + \eta.$$

We then proceed through the proof with this new set, and take  $\eta \rightarrow 0+$  at the end.

compositions of the Lipschitz functions  $\bar{d}_n$  and  $\bar{d}_n$  with the respective distance functions). Hence, by Rademacher's Theorem,  $d_n \in H^1(B; \mathbb{R})$ . Going forward, we will abuse notation by writing  $\bar{d}_n(\text{dist}(x, \Gamma \setminus \mathcal{N}_\rho(I)))$  as  $\bar{d}_n(x)$ , with similar abuse of notation for  $\bar{d}_n(x)$ .

7. Now, we show that the sequences  $(u_n)_n$  and  $(d_n)_n$  are indeed recovery sequences. As in the proof of Theorem 1(i), we let  $\Pi_\epsilon^e$  and  $\Pi_\epsilon^f$  be the two functionals in (7). Then, for the elastic energy

$$\Pi_{\epsilon_n}^e [u_n, d_n] = \Pi_{\epsilon_n}^e [u, d_n, B \setminus \mathcal{N}_{\alpha_n}(\Gamma)] + \Pi_{\epsilon_n}^e [u_n, 1, B \cap \mathcal{N}_{\alpha_n}(\Gamma)],$$

where we have used that  $u_n \equiv u$  in  $B \setminus \mathcal{N}_{\alpha_n}(\Gamma)$  and the fact that  $d_n \equiv 1$  in  $\mathcal{N}_{\alpha_n}(\Gamma)$ .

8. For the first term,

$$\Pi_{\epsilon_n}^e [u, d_n, B \setminus \mathcal{N}_{\alpha_n}(\Gamma)] \leq (1 + k_{\epsilon_n}) \int_{B \setminus \mathcal{N}_{\alpha_n}(\Gamma)} W(x, \epsilon(u)) \, dx \leq (1 + k_{\epsilon_n}) \int_{B \setminus \Gamma} W(x, \epsilon(u)) \, dx,$$

where the first inequality follows from the bounds on  $d_n$  (so that  $(1 - d_n)^2 \leq 1$ ) and the second inequality follows from integrating a non-negative function over nested domains. Taking the limit as  $n \rightarrow \infty$ , we get

$$\limsup_{n \rightarrow \infty} \Pi_{\epsilon_n}^e [u, d_n, B \setminus \mathcal{N}_{\alpha_n}(\Gamma)] \leq \int_{B \setminus \Gamma} W(x, \epsilon(u)) \, dx.$$

9. Meanwhile, for the second term, we first note that

$$\nabla u_n(x) = \left( \frac{2\text{dist}(x, \Gamma)}{\alpha_n} - 1 \right) \nabla u(x) + \frac{2}{\alpha_n} u(x) \otimes \nabla \text{dist}(x, \Gamma)$$

when  $x \in \mathcal{N}_{\alpha_n}(\Gamma) \setminus \mathcal{N}_{\alpha_n/2}(\Gamma)$ . Because  $W(x, \epsilon(u))$  is a quadratic function of  $\nabla u$ , we must have that<sup>10</sup>

$$W(x, \epsilon(u_n)) \leq 2 \left( \frac{2\text{dist}(x, \Gamma)}{\alpha_n} - 1 \right)^2 W(x, \epsilon(u)) + 2C_1 \frac{4}{\alpha_n^2} \|u\|_{L^\infty(B; \mathbb{R}^2)}^2,$$

where the constant  $C_1$  depends on the elastic properties of the bulk material. In computing the previous constant, we used that  $|\nabla \text{dist}(x, \Gamma)| = 1$  almost everywhere in  $B$ , so that  $|u \otimes \nabla \text{dist}(x, \Gamma)| \leq \|u\|_{L^\infty(B; \mathbb{R}^2)}$ . Hence, also noting that the prefactor  $2\text{dist}(x, \Gamma)/\alpha_n - 1 \leq 1$ ,

$$\begin{aligned} \Pi_{\epsilon_n}^e [u_n, 1, B \cap \mathcal{N}_{\alpha_n}(\Gamma)] &\leq 2k_{\epsilon_n} \int_{B \cap \mathcal{N}_{\alpha_n}(\Gamma) \setminus \mathcal{N}_{\alpha_n/2}(\Gamma)} W(x, \epsilon(u)) \, dx \\ &\quad + 8C_1 \frac{k_{\epsilon_n} \|u\|_{L^\infty(B; \mathbb{R}^2)}^2}{\alpha_n^2} \mathcal{L}^2(B \cap \mathcal{N}_{\alpha_n}(\Gamma) \setminus \mathcal{N}_{\alpha_n/2}(\Gamma)), \\ &\leq 2k_{\epsilon_n} \int_{B \cap \mathcal{N}_{\alpha_n}(\Gamma)} W(x, \epsilon(u)) \, dx + 8C_1 \frac{k_{\epsilon_n} \|u\|_{L^\infty(B; \mathbb{R}^2)}^2}{\alpha_n^2} \mathcal{L}^2(\mathcal{N}_{\alpha_n}(\Gamma)). \end{aligned}$$

10. To bound  $\mathcal{L}^2(\mathcal{N}_{\alpha_n}(\Gamma))$ , we appeal to the Minkowski content:

$$\lim_{\alpha \rightarrow 0^+} \frac{\mathcal{L}^2(\mathcal{N}_\alpha(\Gamma))}{2\alpha}$$

which coincides with  $\mathcal{H}^1(\Gamma)$  for closed, rectifiable subsets of  $\mathbb{R}^2$  (Federer, 1996, Theorem 3.2.39). From the fact that this is a convergent, non-negative sequence when evaluated on  $(\alpha_n)_n$ , we observe that there must exist a constant  $C_2 > 0$  such that

$$\mathcal{L}^2(\mathcal{N}_{\alpha_n}(\Gamma)) \leq 2\alpha_n C_2$$

holds for all  $n$ . Hence,

$$\Pi_{\epsilon_n}^e [u_n, 1, B \cap \mathcal{N}_{\alpha_n}(\Gamma)] \leq 2k_{\epsilon_n} \int_{B \cap \mathcal{N}_{\alpha_n}(\Gamma)} W(x, \epsilon(u)) \, dx + 16C_1 C_2 \frac{k_{\epsilon_n} \|u\|_{L^\infty(B; \mathbb{R}^2)}^2}{\alpha_n}.$$

The first term must shrink to zero, because  $B \cap \mathcal{N}_{\alpha_n}(\Gamma) \subseteq B$ ,  $0 \leq \int_B W(x, \epsilon(u)) \, dx < \infty$ , and  $k_{\epsilon_n} \rightarrow 0$  as  $n \rightarrow \infty$ . The second term must also shrink to zero since we have selected  $(\alpha_n)_n$  so that  $k_{\epsilon_n} = o(\alpha_n)$ . Hence,

$$\limsup_{n \rightarrow \infty} \Pi_{\epsilon_n}^e [u_n, 1, B \cap \mathcal{N}_{\alpha_n}(\Gamma)] = 0.$$

<sup>10</sup>  $W(x, \epsilon(u))$  may be shown to have the form  $\nabla u : \tilde{\mathbb{C}}(x) : \nabla u$ , where the symmetric, fourth-order tensor  $\tilde{\mathbb{C}}(x)$  is bounded and has nonnegative components. For such quadratic forms, if  $\nabla u = U_1 + U_2$ , then

$$(U_1 + U_2) : \tilde{\mathbb{C}}(x) : (U_1 + U_2) \leq 2U_1 : \tilde{\mathbb{C}}(x) : U_1 + 2U_2 : \tilde{\mathbb{C}}(x) : U_2.$$

Noting that  $U_1 = f(x)\nabla u$  gives  $2U_1 : \tilde{\mathbb{C}}(x) : U_1 = 2f(x)^2 W(x, \epsilon(u))$ . Meanwhile, by the boundedness of  $\tilde{\mathbb{C}}(x)$ , there exists a constant  $C_1 > 0$  such that  $U_2 : \tilde{\mathbb{C}}(x) : U_2 \leq C_1 |U_2|^2$ .

11. Next, we turn to the surface energy. Define the set

$$A_n = \left\{ \mathbf{x} \in B : d_n(\mathbf{x}) = \bar{d}_n(\mathbf{x}) \right\}.$$

Then

$$\Pi_{\varepsilon_n}^f[\mathbf{u}_n, d_n, B] = \Pi_{\varepsilon_n}^f[\mathbf{u}_n, \bar{d}_n, B \setminus A_n] + \Pi_{\varepsilon_n}^f[\mathbf{u}_n, \bar{d}_n, A_n].$$

12. For integration on  $B \setminus A_n$ , we use the fact that  $g_\varepsilon(\mathbf{x}) \leq g_b$  for any  $\mathbf{x} \in B$ , while  $B \setminus A_n \subseteq B$ , and so

$$\Pi_{\varepsilon_n}^f[\mathbf{u}_n, \bar{d}_n, B \setminus A_n] \leq \int_{B \setminus A_n} \frac{g_b}{2} \left( \frac{\bar{d}_n^2}{\varepsilon_n} + \varepsilon_n |\nabla \bar{d}_n|^2 \right) d\mathbf{x} \leq \int_B \frac{g_b}{2} \left( \frac{\bar{d}_n^2}{\varepsilon_n} + \varepsilon_n |\nabla \bar{d}_n|^2 \right) d\mathbf{x}.$$

The set  $\Gamma \setminus \mathcal{N}_\rho(I)$  is closed and rectifiable. Hence, the integral on the right is simply the one that results from Chambolle's construction for the crack set  $\Gamma \setminus \mathcal{N}_\rho(I)$ . Repeating his steps, we get

$$\limsup_{n \rightarrow \infty} \Pi_{\varepsilon_n}^f[\mathbf{u}_n, \bar{d}_n, B \setminus A_n] \leq \limsup_{n \rightarrow \infty} \int_B \frac{g_b}{2} \left( \frac{\bar{d}_n^2}{\varepsilon_n} + \varepsilon_n |\nabla \bar{d}_n|^2 \right) d\mathbf{x} \leq g_b \mathcal{H}^1(\Gamma \setminus \mathcal{N}_\rho(I)).$$

13. For integration on  $A_n$ , we consider the subsets  $(A_{nj})_j$ , where

$$A_{nj} = \left\{ \mathbf{x} \in A_n : d_n(\mathbf{x}) = \bar{d}_{nj}(\mathbf{x}) \right\},$$

where we use the shorthand  $\bar{d}_{nj}(\mathbf{x}) := \bar{d}_n(\text{dist}(\mathbf{x}, \Gamma_j))$ . We recall that the simply connected pieces  $(\Gamma_j)_j$  which compose  $\Gamma \cap I$  were defined in Step 1. Then, because these subsets might overlap (in particular, if  $\bar{d}_{nj}(\mathbf{x}) = \bar{d}_{nk}(\mathbf{x}) = 1$  for some  $j \neq k$ ),

$$\Pi_{\varepsilon_n}^f[\mathbf{u}_n, \bar{d}_n, A_n] \leq \sum_{j=1}^J \Pi_{\varepsilon_n}^f[\mathbf{u}_n, \bar{d}_{nj}, A_{nj}]$$

Additionally, because  $\bar{d}_{nj}(\mathbf{x}) = 0$  for  $\mathbf{x} \notin \mathcal{N}_\rho(\Gamma_j)$ , we have  $A_{nj} \subseteq \mathcal{N}_\rho(\Gamma_j)$ , and so for each  $j$

$$\Pi_{\varepsilon_n}^f[\mathbf{u}_n, \bar{d}_{nj}, A_{nj}] \leq \Pi_{\varepsilon_n}^f[\mathbf{u}_n, \bar{d}_{nj}, \mathcal{N}_\rho(\Gamma_j)] = \int_{\mathcal{N}_\rho(\Gamma_j)} \frac{g_{\varepsilon_n}(\mathbf{x})}{2} \left( \frac{\bar{d}_{nj}^2}{\varepsilon_n} + \varepsilon_n |\nabla \bar{d}_{nj}|^2 \right) d\mathbf{x}.$$

Finally, because  $\text{dist}(\mathbf{x}, \Gamma_j) \geq \text{dist}(\mathbf{x}, I)$ , we have  $g_\varepsilon(\mathbf{x}) = \bar{g}(\text{dist}(\mathbf{x}, I)/\varepsilon) \leq \bar{g}(\text{dist}(\mathbf{x}, \Gamma_j)/\varepsilon)$ , and so

$$\int_{\mathcal{N}_\rho(\Gamma_j)} \frac{g_{\varepsilon_n}(\mathbf{x})}{2} \left( \frac{\bar{d}_{nj}^2}{\varepsilon_n} + \varepsilon_n |\nabla \bar{d}_{nj}|^2 \right) d\mathbf{x} \leq \int_{\mathcal{N}_\rho(\Gamma_j)} \frac{\bar{g}(\text{dist}(\mathbf{x}, \Gamma_j)/\varepsilon_n)}{2} \left( \frac{\bar{d}_{nj}^2}{\varepsilon_n} + \varepsilon_n |\nabla \bar{d}_{nj}|^2 \right) d\mathbf{x}.$$

14. Let  $z = \text{dist}(\mathbf{x}, \Gamma_j)$ . Then  $\bar{d}_{nj}(\mathbf{x}) = \bar{d}_n(z)$ . Meanwhile,  $\nabla \bar{d}_{nj}(\mathbf{x}) = \bar{d}'_n(z) \nabla \text{dist}(\mathbf{x}, \Gamma_j)$ , where we recall that  $|\nabla \text{dist}(\mathbf{x}, \Gamma_j)| = 1$  almost everywhere, and so  $|\nabla \bar{d}_{nj}(\mathbf{x})|^2 = (\bar{d}'_n(z))^2$  almost everywhere. Hence, the above integrand depends only on  $z$ , the distance to  $\Gamma_j$ . Via integration over level sets of the distance function (Evans and Gariepy, 2015, Theorem 3.11), this may be written as

$$\int_{\mathcal{N}_\rho(\Gamma_j)} \frac{\bar{g}(\text{dist}(\mathbf{x}, \Gamma_j)/\varepsilon_n)}{2} \left( \frac{\bar{d}_{nj}^2}{\varepsilon_n} + \varepsilon_n |\nabla \bar{d}_{nj}|^2 \right) d\mathbf{x} = \int_0^\rho \frac{\bar{g}(z/\varepsilon_n)}{2} \left( \frac{\bar{d}_n(z)^2}{\varepsilon_n} + \varepsilon_n (\bar{d}'_n(z))^2 \right) \mathcal{H}^1(\partial \mathcal{N}_z(\Gamma_j)) dz.$$

Using Proposition 4, we may bound

$$\begin{aligned} & \int_0^\rho \frac{\bar{g}(z/\varepsilon_n)}{2} \left( \frac{\bar{d}_n(z)^2}{\varepsilon_n} + \varepsilon_n (\bar{d}'_n(z))^2 \right) \mathcal{H}^1(\partial \mathcal{N}_z(\Gamma_j)) dz \\ & \leq \left( 4\pi\rho + 2 \left( 1 + \frac{\rho}{R_{\min}} \right) \mathcal{H}^1(\Gamma_j) \right) \int_0^\rho \frac{\bar{g}(z/\varepsilon_n)}{2} \left( \frac{\bar{d}_n(z)^2}{\varepsilon_n} + \varepsilon_n (\bar{d}'_n(z))^2 \right) dz. \end{aligned}$$

The integral on the right is precisely that which is minimized by our choice of  $\bar{d}_n$ . Hence,

$$\lim_{n \rightarrow \infty} \int_0^\rho \frac{\bar{g}(z/\varepsilon_n)}{2} \left( \frac{\bar{d}_n(z)^2}{\varepsilon_n} + \varepsilon_n (\bar{d}'_n(z))^2 \right) dz = \frac{g_{\text{int}}}{2}.$$

As a shorthand, let  $g_n/2$  be the above integral for integer  $n$ , so that  $\lim_{n \rightarrow \infty} g_n = g_{\text{int}}$ .

15. Putting together the bounds for the integrals over each set  $A_{n_j}$ , we conclude that

$$\begin{aligned} \limsup_{n \rightarrow \infty} \Pi_{\varepsilon_n}^f[\mathbf{u}_n, \bar{d}_n, A_n] &\leq \lim_{n \rightarrow \infty} \sum_{j=1}^J \frac{g_n}{2} \left( 4\pi\rho + 2 \left( 1 + \frac{\rho}{R_{\min}} \right) \mathcal{H}^1(\Gamma_j) \right) \\ &= \lim_{n \rightarrow \infty} g_n \left( 2\pi J\rho + \left( 1 + \frac{\rho}{R_{\min}} \right) \sum_{j=1}^J \mathcal{H}^1(\Gamma_j) \right) \\ &= g_{\text{int}} \left( 2\pi J\rho + \left( 1 + \frac{\rho}{R_{\min}} \right) \mathcal{H}^1(\Gamma \cap I) \right). \end{aligned}$$

16. Finally, putting together Steps 8, 10, 12, and 15 yields

$$\limsup_{n \rightarrow \infty} \Pi_{\varepsilon_n}[\mathbf{u}_n, d_n] \leq \int_{B \setminus \Gamma} W(\mathbf{x}, \varepsilon(\mathbf{u})) \, dx + g_b \mathcal{H}^1(\Gamma \setminus \mathcal{N}_\rho(I)) + g_{\text{int}} \left( 2\pi J\rho + \left( 1 + \frac{\rho}{R_{\min}} \right) \mathcal{H}^1(\Gamma \cap I) \right).$$

Since  $\rho > 0$  is arbitrary, we may take it to zero to yield the conclusion. In particular, for the second term, we note that

$$\bigcup_{\rho > 0} \Gamma \setminus \mathcal{N}_\rho(I) = \Gamma \setminus I$$

and so by continuity of measures on nested sets

$$\lim_{\rho \rightarrow 0^+} \mathcal{H}^1(\Gamma \setminus \mathcal{N}_\rho(I)) = \mathcal{H}^1(\Gamma \setminus I). \quad \square$$

### 5. Numerical implementation

The model and analysis of the previous sections does not address crack evolution in response to time-varying external loads. Rather, the variational principle itself is general, providing a framework to study problems with interfaces. In the following sections, we apply our approach to problems featuring crack growth in order to study toughening mechanisms in SBs. While a crack growth model is not part of our theoretical framework, for concreteness we summarize the approach used in the computations. For further details of the model and method, we refer the reader to Vijaykumar (2019).

#### 5.1. Evolution via local stationary points

We suppose that the applied displacements vary with time  $t$  (i.e.,  $\hat{\mathbf{u}} = \hat{\mathbf{u}}(t)$ ). Then, at time  $t$ , we seek  $(\mathbf{u}(t), d(t))$  to be stationary points of the functional  $\Pi_\varepsilon$ . That is, recalling the admissible function spaces

$$\mathcal{U}_u(t) = \{ \mathbf{v} \in H^1(B; \mathbb{R}^2) : \mathbf{v}(\mathbf{x}) = \hat{\mathbf{u}}(t, \mathbf{x}) \text{ for } \mathbf{x} \in \partial B_u \} \tag{17a}$$

$$\mathcal{U}_d = H^1(B; \mathbb{R}), \tag{17b}$$

and defining test spaces

$$\mathcal{V}_u = \{ \mathbf{v} \in H^1(B; \mathbb{R}^2) : \mathbf{v} \equiv \mathbf{0} \text{ on } \partial B_u \} \tag{18a}$$

$$\mathcal{V}_d = \mathcal{U}_d, \tag{18b}$$

at time  $t$  we seek  $(\mathbf{u}(t), d(t)) \in \mathcal{U}_u(t) \times \mathcal{U}_d$  which satisfy

$$\begin{aligned} 0 &= \int_B ((1-d)^2 + k_\varepsilon) \frac{\partial W(\mathbf{x}, \varepsilon(\mathbf{u}))}{\partial \varepsilon} : \varepsilon(\mathbf{v}) \, dx \\ &+ \int_B \left\{ \left[ \frac{g_\varepsilon(\mathbf{x})d}{\varepsilon} - 2(1-d)W(\mathbf{x}, \varepsilon(\mathbf{u})) \right] \phi + g_\varepsilon(\mathbf{x})\varepsilon \nabla d \cdot \nabla \phi \right\} \, dx \end{aligned} \tag{19}$$

for any  $(\mathbf{v}, \phi) \in \mathcal{V}_u \times \mathcal{V}_d$ .

We remark that stationarity of  $\Pi_\varepsilon$  is a very different condition from global minimality (Bourdin et al., 2008). Moreover, a consequence of  $\Gamma$ -convergence is that global minimizers of  $\Pi_\varepsilon$  will converge to those of  $\Pi$  as  $\varepsilon \rightarrow 0$  (Dal Maso, 1993); in general, this result does not hold for local minimizers or stationary points.

#### 5.2. Discretization and solution procedure

We partition the time interval of interest  $[0, T]$  into  $N$  steps:  $0 = t_0 < t_1 < \dots < t_N = T$ . For simplicity, we assume a fixed time step  $\Delta t = t_{n+1} - t_n$  for any  $n$ . We seek functions  $(\mathbf{u}_n, d_n)$  which approximate  $(\mathbf{u}(t_n), d(t_n))$ . We spatially discretize the stationarity equation using the Finite Element Method (e.g., Hughes, 2000) with bilinear quadrilateral (Q1) finite elements. In other words, we partition  $B$  into a mesh  $\mathcal{T}^h$  of non-overlapping quadrilaterals with maximum diameter  $h$ ; the admissible and test functions are those that are continuous and whose restriction to any quadrilateral  $E \in \mathcal{T}^h$  are bilinear. We let  $\mathcal{U}_u^h(t_n)$  denote the admissible finite element function space for  $\mathbf{u}$  at  $t_n$ , and we use similar notation for the other function spaces. We construct our mesh  $\mathcal{T}^h$  to conform to the

boundaries of the widened interface (i.e., the  $m\epsilon$ -neighborhood of  $T$ ). This ensures that the restriction of  $g_\epsilon(\mathbf{x})$  to each quadrilateral is a constant (either  $g_b$  or  $g_i$ ).

We define  $(\mathbf{u}_n, d_n) \in \mathcal{U}_u^h(t_n) \times \mathcal{V}_d^h$  to be the functions satisfying (19) for any  $(\mathbf{v}, \phi) \in \mathcal{V}_u^h \times \mathcal{V}_d^h$ . Choosing a set of basis functions for the finite element spaces results in a finite-dimensional system of nonlinear equations. We solve these equations monolithically (simultaneously for both  $\mathbf{u}_n$  and  $d_n$ ) using Newton–Raphson iteration in *Abaqus* (2012). Instead of a monolithic scheme, we could have staggered the solution of  $\mathbf{u}_n$  and  $d_n$  (the so-called “Alternate Minimization” approach Bourdin et al., 2000) to take advantage of the biconvexity of  $\Pi_\epsilon$ .

### 5.3. Modifications to the equations

Motivated by physical modeling considerations, we make three modifications to (19) before use in the examples. First, the previous equations do not distinguish energetically between open cracks and interpenetrated cracks, a symmetry also present in classical fracture mechanics without contact. Hence, cracks may nucleate and grow in regions under compression. To combat this, several approaches have been proposed in the literature (cf. the review Ambati et al., 2015). These approaches split the strain energy density  $W$  into positive and negative parts (corresponding to tensile and compressive strains and/or stresses), and only the positive part is degraded by the damage. That is, we replace

$$((1 - d)^2 + k_\epsilon) W(\mathbf{x}, \epsilon) \rightarrow ((1 - d)^2 + k_\epsilon) W^+(\mathbf{x}, \epsilon) + W^-(\mathbf{x}, \epsilon).$$

In this work, we adopt the spectral split of Miehe et al. (2010b). For the isotropic, linear elastic constitutive response, the forms of  $W^\pm$  are

$$W^\pm(\mathbf{x}, \epsilon) = \frac{1}{2} \lambda(\mathbf{x}) \langle \epsilon_1 + \epsilon_2 \rangle_\pm + \mu(\mathbf{x}) (\langle \epsilon_1 \rangle_\pm^2 + \langle \epsilon_2 \rangle_\pm^2)$$

where  $\epsilon_1$  and  $\epsilon_2$  are the principal strains of the tensor  $\epsilon$ , and  $\langle \epsilon \rangle_+ = \max\{0, \epsilon\}$  while  $\langle \epsilon \rangle_- = \min\{0, \epsilon\}$ .

Second, we impose irreversibility on the crack evolution. We remark that this condition was part of the original VFT (Francfort and Marigo, 1998) and RVFT (Bourdin et al., 2000), though it may not be applicable for all engineering situations (i.e., crack healing). In RVFT, this condition is  $d(t_1, \mathbf{x}) \geq d(t_2, \mathbf{x})$  for any  $t_1 \geq t_2$  and  $\mathbf{x} \in B$ . Numerically, this condition can be enforced via inequality constraint  $(d_{n+1}(\mathbf{x}) \geq d_n(\mathbf{x})$  for  $\mathbf{x} \in B$ ) (Bourdin et al., 2000). We instead adopt the approach of Miehe et al. (2010a), which replaces the strain energy density  $W^+$  in the damage-field portion of (19) with a history variable

$$H(t, \mathbf{x}) = \max_{s \in [0, t]} W^+(\mathbf{x}, \epsilon(\mathbf{u}(s))).$$

In the time-discrete case, this variable is

$$H(t_n, \mathbf{x}) = \max_{0 \leq m < n} W^+(\mathbf{x}, \epsilon(\mathbf{u}_m)).$$

In the formulation in Section 3, we have neglected inertial effects, i.e. we have assumed that the deformation is static. When we introduce time-varying external loading, we maintain the assumption of negligible inertia, which is referred to as quasi-static behavior. Hence, time  $t$  only acts to parameterize the external loads and does not need to correspond to physical time. Rather  $t$  can be replaced by any increasing load parameter. As a consequence of neglecting inertia, numerical instabilities can arise when the damage field evolves rapidly from one time step to another, for example in the case of catastrophic crack propagation, where the crack may grow large distances in very small intervals of time. In particular, conventional methods to solve (19) such as Newton iteration can fail to find solutions because  $(\mathbf{u}_{n+1}, d_{n+1})$  is “far” from  $(\mathbf{u}_n, d_n)$ . To mitigate these numerical instabilities, as the final modification, when seeking  $d_{n+1}$  we add to the damage field Eq. (19) a viscous damping term of the form  $\frac{\eta}{2\Delta t} \left( \frac{d - d_n}{\Delta t} \right) \left| \frac{d - d_n}{\Delta t} \right| \phi$ , where  $\eta > 0$  (Miehe et al., 2010a). This term may be derived by adding the cubic penalty  $\frac{\eta}{6} |d|^3$  to the modified energy (7), introducing the finite time difference  $\dot{d}(t_{n+1}) \approx \frac{d - d_n}{\Delta t}$ , and taking the variation with respect to  $d$ .

In summary, the modified version of (19) incorporating the above three changes is as follows. At time  $t_{n+1}$ , we seek  $(\mathbf{u}, d) \in \mathcal{U}_u^h(t_{n+1}) \times \mathcal{V}_d^h$  which satisfy

$$0 = \int_B \left[ ((1 - d)^2 + k_\epsilon) \frac{\partial W^+(\mathbf{x}, \epsilon(\mathbf{u}))}{\partial \epsilon} + \frac{\partial W^-(\mathbf{x}, \epsilon(\mathbf{u}))}{\partial \epsilon} \right] : \epsilon(\mathbf{v}) \, dx + \int_B \left\{ \left[ \frac{g_\epsilon(\mathbf{x})d}{\epsilon} - 2(1 - d)H(t_{n+1}, \mathbf{x}) + \frac{\eta}{2\Delta t} \left( \frac{d - d_n}{\Delta t} \right) \left| \frac{d - d_n}{\Delta t} \right| \right] \phi + g_\epsilon(\mathbf{x}) \epsilon \nabla d \cdot \nabla \phi \right\} \, dx \tag{20}$$

for any  $(\mathbf{v}, \phi) \in \mathcal{V}_u^h \times \mathcal{V}_d^h$ . We denote the solution to (20) as  $(\mathbf{u}_{n+1}, d_{n+1})$ .

## 6. Numerical verification

In this section, we assess the implementation of the modified RVFT for interfaces (RVFTI) in Section 5 and, in particular, how it relates to the theory of Section 3.3. The verification provided in this section is two-fold:

- (1) In standard RVFT, it has been shown that crack initiation occurs when the energy release rate is equal to the constant fracture toughness  $g$  (Kuhn and Müller, 2010). We show for RVFTI that crack initiation occurs when the energy release rate is equal to  $g_{\text{int}}$  in (8).



- (2) We study the problem of the kinking of a crack at the bi-material interface subjected to far-field loading. We compare the computationally-observed kink angles against those predicted by the semi-analytical solutions of He and Hutchinson (1989). We also study the ability of RVFTI to predict crack trapping by the interface, which we also compare with He and Hutchinson (1989).

### 6.1. Crack initiation fracture toughness for the interface model

We first study a single edge notch (SEN) specimen under plane strain conditions with Young's modulus  $E$  and Poisson's ratio  $\nu$ . The bulk fracture toughness is  $g_b$ , and we set the fracture toughness in the widened interface as  $g_i$ . The specimen has width  $b$ , while the initial notch has length  $a$ . We take the interface thickness to be  $2m\epsilon$ . The specimen is depicted in Fig. 3(a).

We prescribe along the boundary of the specimen the asymptotic mode I displacement field with prescribed stress intensity factor  $K_I^\infty$  (see Anderson, 2005)

$$u_x(\mathbf{x}) = K_I^\infty u_x^I(\mathbf{x}) = \frac{K_I^\infty}{2\mu} \sqrt{\frac{r}{2\pi}} \cos\left(\frac{\theta}{2}\right) (3 - 4\nu - \cos(\theta)), \quad (21a)$$

$$u_y(\mathbf{x}) = K_I^\infty u_y^I(\mathbf{x}) = \frac{K_I^\infty}{2\mu} \sqrt{\frac{r}{2\pi}} \sin\left(\frac{\theta}{2}\right) (3 - 4\nu - \cos(\theta)), \quad (21b)$$

where  $r$  and  $\theta$  are the usual polar coordinates associated with the point  $\mathbf{x} \in \mathbb{R}^2$ . Under plane strain conditions, the energy release rate  $\mathcal{G}$  is related to  $K_I^\infty$  via  $\mathcal{G} = (1 - \nu^2)(K_I^\infty)^2/E$ .

From Griffith's criterion (Griffith, 1921), crack growth occurs when the energy release rate at the crack tip is equal to the fracture toughness of the material, i.e.  $\mathcal{G} = g_{\text{int}}^h$ . Hence, from a simulation we may estimate the interface fracture toughness, denoted by  $g_{\text{int}}^h$ , using the relationship

$$g_{\text{int}}^h = \frac{1 - \nu^2}{E} (K_{I,\text{cr}}^\infty)^2, \quad (22)$$

where  $K_{I,\text{cr}}^\infty$  is the critical value of the prescribed mode I stress intensity factor at which the crack initiates.

In our computations,  $b = 100$  mm,  $a = b/4$ , and we took the height of the SEN specimen to be  $100b$ . The material has shear modulus  $\mu = 22 \times 10^3$  MPa and Poisson's ratio  $\nu = 1/4$ . For the damage field, we set  $\epsilon = b/500$ ,  $k_\epsilon = 0$ , and we vary  $m \in \{0.1, 0.2, 0.3, 0.4, 0.5\}$ ,  $g_i \in \{1, 5\}$  N/mm, and  $g_b/g_i \in \{2, 5, 20\}$ .

For the finite-width notch, we initialize the damage field by setting  $d = 1$  in the rectangle  $-a \leq x \leq 0$  and  $-h \leq y \leq h$ , where  $h = b/1000$  is the half-width of the notch. We estimate  $K_{I,\text{cr}}^\infty$  for the above parameter combinations by slowly incrementing the parameter  $K_I^\infty$  from zero until the first node ahead of the notch (at  $x = 0$ ) attains a damage value of  $d = 0.99$ . These values of  $K_{I,\text{cr}}^\infty$  are then used to estimate  $g_{\text{int}}^h$  in (22).

In Fig. 3(b), we compare the analytical expression for the ratio  $g_{\text{int}}/g_b$  of (8) against the numerically computed value  $g_{\text{int}}^h/g_b$ . The thick line with unit slope corresponds to one-to-one equivalence. We observe good agreement between  $g_{\text{int}}^h$  and  $g_{\text{int}}$ , and the error between the two is within  $0.065g_b$ . Additionally the precise values of  $g_i$  and  $g_b$  had minimal impact on  $g_{\text{int}}^h/g_b$ , which is consistent with (8). Hence, we conclude that the numerically obtained values for interface fracture toughness are largely consistent with their analytical counterparts.

For the cases where  $m = 0.2$  and  $g_i = 1$  N/mm, we also ran simulations with variable  $\epsilon$ . We show the computed values of  $g_{\text{int}}^h/g_b$  versus  $\epsilon$  in Fig. 3(c). All simulations results in this subfigure were computed on a single mesh with  $h \approx 0.01$  mm. We observe that as  $\epsilon$  decreases, the value of  $g_{\text{int}}^h$  gets closer to the exact value  $g_{\text{int}}$ . Because of the differences between RVFTI in Section 5 and the theory in Section 4, and several other differences, it is not guaranteed that the numerical simulations should converge under  $\epsilon$  refinement. For these reasons, we find the results in Fig. 3(c) especially remarkable.

### 6.2. Kinking of a crack at a bi-material interface

We benchmark RVFTI by comparing against kink angle predictions made by He and Hutchinson (1989) for a semi-infinite crack along the interface between two materials and subjected to far-field loading. The geometry of the crack is illustrated in Fig. 4, where a semi-infinite crack is present along the interface of material 1 and 2. The shear modulus and Poisson's ratio of materials 1 and 2 are  $(\mu_1, \nu_1)$  and  $(\mu_2, \nu_2)$ , respectively.

He and Hutchinson assume that a new crack grows from the tip of the semi-infinite crack along a fixed direction. In this section, the original semi-infinite crack is termed the interface crack and the new crack segment is termed the kinked crack. The angle that the kinked crack makes with respect to the interface (measured clockwise from the  $x$ -axis) is called the kink angle  $\omega$  and its length is denoted as  $a$ .

The domain is loaded at infinity so that the interface crack (without the kink) is under a state of mode I and mode II stress intensity; these remote stress intensity factors are denoted  $K_1$  and  $K_2$ , respectively. Following He and Hutchinson (1989), the mode mixity is described using a non-dimensional parameter called the phase angle  $\gamma = \arctan(K_2/K_1)$ . The parameter  $\gamma$  indicates whether the loading is mode I or mode II dominant;  $\gamma = 0$  under pure mode I loading, while  $\gamma = \pi/2$  for pure mode II loading, and  $\gamma < \pi/4$  (resp.  $\gamma > \pi/4$ ) for mode I (resp. mode II) dominant loading. Expressions for the asymptotic mode I and mode II displacement fields in the vicinity of the interface crack in terms of  $K_1$  and  $K_2$  will be described later.

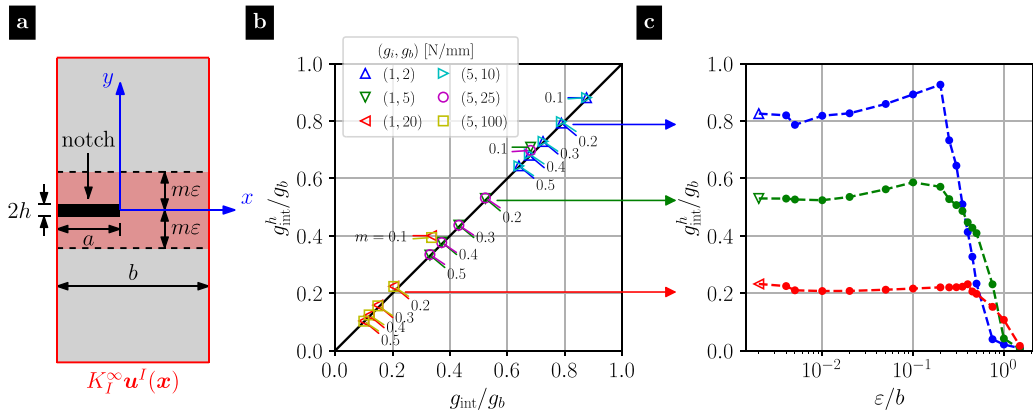


Fig. 3. (a) Schematic of SEN specimen subjected to the asymptotic mode I displacement field along the boundary. The specimen has width  $b$ , the initial notch has length  $a = b/4$ , and the interface thickness is  $2m\epsilon$ . (b) Comparison between the theoretical interface fracture toughness,  $g_{int}/g_b$ , and that computed from the simulations,  $g_{int}^h/g_b$ , for  $m \in \{0.1, 0.2, 0.3, 0.4, 0.5\}$ ,  $\epsilon = b/500$ ,  $g_i \in \{1, 5\}$  N/mm and  $g_b/g_i \in \{2, 5, 20\}$ . (c) Variation in the computed value of  $g_{int}^h/g_b$  versus  $\epsilon$  for the cases where  $m = 0.2$  and  $g_i = 1$  N/mm.

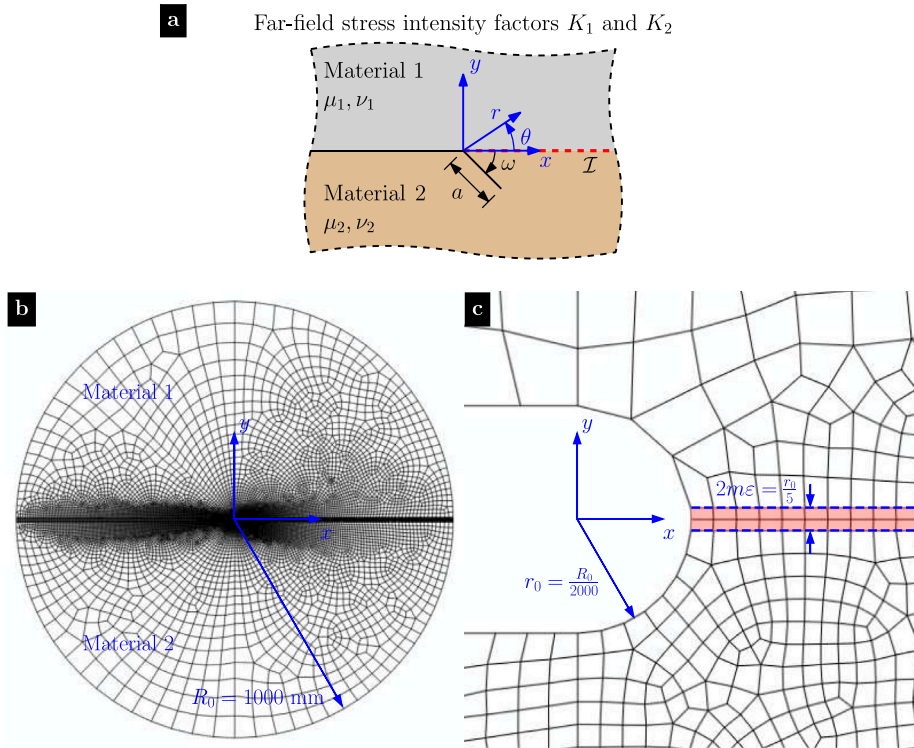


Fig. 4. Semi-infinite crack along a bi-material interface. (a) Schematic of the geometry, showing a crack along the interface between materials 1 (gray) and 2 (brown), which has kinked by an angle  $\omega$  (defined clockwise) into material 2. The far-field loading is characterized by stress intensity factors  $K_1$  and  $K_2$  with stress intensity phase angle  $\gamma = \arctan(K_2/K_1)$ . The kink length  $a$  is assumed to be very small compared to any other relevant problem dimensions. (b) Quadrilateral mesh used in the finite element computations. The computational domain has radius  $R_0 = 1000$  mm and finite-width notch. (c) Closeup of the notch tip, showing the notch radius  $r_0 = R_0/2000$ , and the wide interface with width  $2m\epsilon = r_0/5$ .

For the bi-material problem studied in He and Hutchinson (1989), it had been shown that the kink angle depends on two non-dimensional material parameters called the Dundurs mismatch parameters  $\alpha$  and  $\beta$  (Dundurs, 1969), which depend as follows on the four material moduli:

$$\alpha := \frac{\mu_1(1 - \nu_2) - \mu_2(1 - \nu_1)}{\mu_1(1 - \nu_2) + \mu_2(1 - \nu_1)}, \tag{23a}$$

$$\beta := \frac{1}{2} \left( \frac{\mu_1 (1 - 2\nu_2) - \mu_2 (1 - 2\nu_1)}{\mu_1 (1 - \nu_2) + \mu_2 (1 - \nu_1)} \right). \tag{23b}$$

The parameter  $\alpha$  can be interpreted as a relative measure of stiffness;  $\alpha = 1$  when material 1 is rigid and  $\alpha = -1$  when material 2 is rigid. Physical interpretation for  $\beta$  is unclear. In this work we choose  $\beta = 0$  because for the case of  $\beta \neq 0$  it has been shown that the interface crack faces interpenetrate (Comninou, 1977; Rice, 1988; Anderson, 1988), which is unphysical.

The mode I and II stress intensity factors of the kinked crack are denoted by  $K_I$  and  $K_{II}$ , respectively. They may be related to the remote stress intensity factors,  $K_1$  and  $K_2$ , for the case of  $\beta = 0$ , as given in He and Hutchinson (1989),

$$K_I + iK_{II} = (c(\omega, \alpha) + \bar{d}(\omega, \alpha)) K_1 + i(c(\omega, \alpha) - \bar{d}(\omega, \alpha)) K_2, \tag{24}$$

where  $i = \sqrt{-1}$ . The functions  $c$  and  $d$  are complex-valued in terms of  $\omega$  and  $\alpha$ , and the symbol  $(\bar{\cdot})$  denotes the complex conjugate.

### 6.2.1. Analytical results

The procedure employed in He and Hutchinson (1989) to predict the kink angle for a given loading  $\gamma$  and  $\alpha$  (and particularized to  $\beta = 0$ ) is briefly reviewed. For a given loading  $\gamma$ , the interface crack is assumed to have kinked by an angle  $\omega$ , forming an extended crack of length  $a$ . The kinked crack surfaces are free of traction. In He and Hutchinson (1989), the kinked crack is considered to be a distribution of edge dislocations. To enforce traction free conditions on the kinked crack segment, the stress fields from the interface crack and the distribution of edge dislocations are superimposed and set to zero. This leads to a singular integral equation which is solved numerically using Chebyshev polynomials. The complex valued functions  $c$  and  $d$  are tabulated for different values of  $\omega$ . The energy release rate  $\mathcal{G}$ , given by

$$\mathcal{G} = q^{-2} \mathcal{G}_0 [ |c|^2 + |d|^2 + 2\Re(cde^{2i\gamma}) ], \tag{25}$$

is computed as a function of  $\omega$ , where  $|\cdot|$  denotes the magnitude of a complex number. In this equation, the symbol  $q := \sqrt{1/(1 + \alpha)}$ , the symbol  $\mathcal{G}_0$  is the energy release rate of the interface crack and the symbol  $\Re(\cdot)$  is the real part of complex number. A crack propagation criterion is necessary to specify the kink angle  $\omega$ . In He and Hutchinson (1989), the crack is assumed to kink in the direction that maximizes  $\mathcal{G}$  for a given  $\alpha$  and  $\gamma$ . This condition is called the maximum energy release rate (MER) criterion. The optimal kink angle is denoted by  $\hat{\omega}$ . For a given  $\gamma$  and  $\alpha$ , the kink angle  $\hat{\omega}$  can be computed by setting  $d\mathcal{G}/d\omega|_{\omega=\hat{\omega}} = 0$  for  $d^2\mathcal{G}/d\omega^2|_{\omega=\hat{\omega}} < 0$ .

To compute  $\hat{\omega}$  from (25), the functional form of the complex valued functions  $c(\omega, \alpha)$  and  $d(\omega, \alpha)$  are necessary. No analytical solution exists, so one would need to solve the singular integral equation as in He and Hutchinson (1989) and tabulate the coefficients for  $c(\omega, \alpha)$  and  $d(\omega, \alpha)$ . To circumvent this issue, Veljkovic (2005) proposed closed form approximations to the complex valued functions  $c(\omega, \alpha)$  and  $d(\omega, \alpha)$ , given as

$$c(\omega, \alpha) \approx \frac{1}{2} \sqrt{\frac{1}{1 + \alpha}} \left( e^{-\frac{i\omega}{2}} + e^{-\frac{3i\omega}{2}} \right), \tag{26a}$$

$$d(\omega, \alpha) \approx \frac{1}{4} \sqrt{\frac{1}{1 - \alpha}} \left( e^{-\frac{i\omega}{2}} - e^{\frac{3i\omega}{2}} \right). \tag{26b}$$

We reiterate that the prior expressions are specialized for the case of  $\beta = 0$ .

We evaluate the accuracy of the approximate functions given in (26) by computing the kink angles for the cases of  $\alpha = \{0, 0.25, 0.5\}$  and comparing them to those computed with the tabulated data provided in He and Hutchinson (1989). In Fig. 5(a), we plot the computed kink angles as a function of phase angle  $\gamma$  using the tabulated data of He and Hutchinson (1989) and the approximate functions (Veljkovic, 2005) for  $\alpha = 0$ . The tabulated data and approximate functions produce similar kink angles  $\hat{\omega}$ , particularly at low  $\gamma$ . We also plot the kink angles for  $\alpha = 0.25$  and  $0.5$  in Figs. 5(b) and (c), respectively. The values of  $\hat{\omega}$  computed using the approximate functions of Veljkovic (2005) are less accurate for  $\alpha = 0.5$  than for  $\alpha = 0$  or  $\alpha = 0.25$ . Thus, we can conclude that the approximate closed form solutions for  $c(\omega, \alpha)$  and  $d(\omega, \alpha)$  given in (26) should not be used for  $\alpha > 0.5$ .

### 6.2.2. Simulations with RVFTI

To benchmark RVFTI, we propose to compute the kink angles for an interface crack for  $\alpha = \{0, 0.25, 0.5\}$  and  $0 \leq \gamma \leq \pi/4$ . We consider a circular domain as shown in Fig. 4(b), where the interface crack is modeled as a notch whose length is equal to that of the radius  $R_0 = 1000$  mm. The region above the notch is material 1 and the region below the notch is material 2. An enlarged view of the notch root is shown in Fig. 4(c), along with a local polar coordinate system attached to the notch tip. Contrary to polar angle  $\theta$ , we measure kink angle  $\hat{\omega}$  clockwise with respect to the  $x$ -axis. The notch root radius is  $r_0 = R_0/2000$ . For the phase-field model, we select  $\epsilon = r_0$  and  $k_\epsilon = 2.5 \times 10^{-4}$ , while the widened interface ahead of the notch has width  $m\epsilon = r_0/10 = R_0/20000$ .

We set  $\mu_1 = 1000$  MPa and  $\nu_1 = 0.3$  for material 1, while the elastic parameters for material 2 are determined from  $\beta = 0$  and  $\alpha \in \{0, 0.25, 0.5\}$ . We assign to both materials an identical bulk fracture toughness  $g_b$ , while the widened interface has fracture toughness  $g_i$ . The values of  $g_b$  and  $g_i$  are chosen to ensure that the crack will always kink into material 2 (see He and Hutchinson, 1989 for details).

Along the outer boundary (at  $r = R_0$ , a sufficient distance from the notch tip), the domain is subjected to the asymptotic displacement fields for an interface crack. With  $\beta = 0$ , these may be written in complex notation as

$$u_x + iu_y = \frac{|K| \sqrt{R_0}}{\mu_1} \sqrt{\frac{1}{8\pi}} \left( (3 - 4\nu_1) e^{i\left(\frac{\theta}{2} - \gamma\right)} - e^{-i\left(\frac{\theta}{2} + \gamma\right)} - i \sin \theta e^{i\left(\frac{\theta}{2} + \gamma\right)} \right), \tag{27a}$$

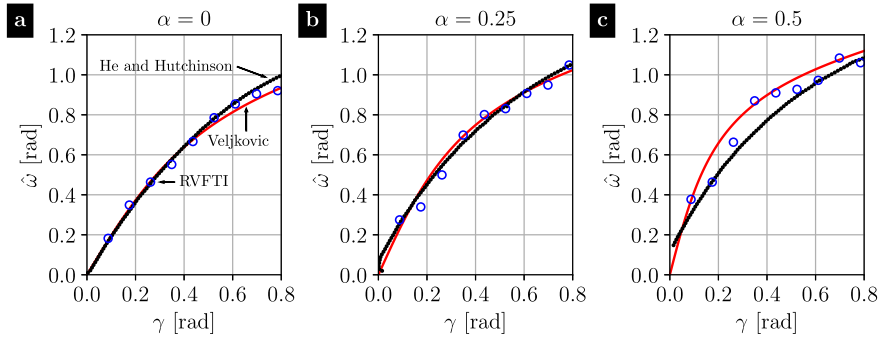


**Fig. 5.** Theoretical and computed kink angles  $\hat{\omega}$  versus mode mixity  $\gamma = \tan(K_2/K_1)$  for a crack at a bi-material interface with Dundurs mismatch parameters  $\beta = 0$  and (a)  $\alpha = 0$ , (b)  $\alpha = 0.25$ , and (c)  $\alpha = 0.5$ . The black circles show the theoretical angles computed from (25) using tabulated values of  $c(\omega, \alpha)$  and  $d(\omega, \alpha)$  from He and Hutchinson (1989). The red lines show the theoretical angles computing using approximations of  $c(\omega, \alpha)$  and  $d(\omega, \alpha)$  in (26). The blue circles are the kink angles observed in the simulations using RVFTI.

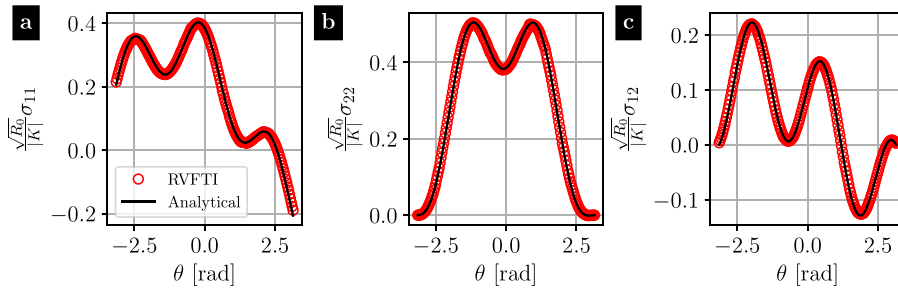


**Fig. 6.** Variation of the far-field stress components versus polar angle  $\theta$ . The red circles show the data obtained from a simulation using RVFTI with  $\alpha = 0.25$  and  $\gamma = \pi/12$ . The black lines are the analytical formula in (28).

for material 1, and

$$u_x + iu_y = \frac{|K|\sqrt{R_0}}{\mu_2} \sqrt{\frac{1}{8\pi}} \left( (3 - 4\nu_2) e^{i(\frac{\theta}{2} - \gamma)} - e^{-i(\frac{\theta}{2} + \gamma)} - i \sin \theta e^{i(\frac{\theta}{2} + \gamma)} \right) \quad (27b)$$

for material 2, where  $|K| = \sqrt{K_1^2 + K_2^2}$ . The individual displacement components  $u_x$  or  $u_y$  are extracted from (27) as the real or imaginary parts of the previous equations, respectively. In our simulations, for each  $\gamma$ , we slowly increase the stress intensity magnitude  $|K|$  until a crack nucleates at the notch tip and grows into material 2.

The presence of a non-zero notch root radius and the phase-field length scale  $\epsilon$  slightly alters the stress field around the crack tip. However, by choosing these dimensions to be small compared with  $R_0$ , the alteration to the stress field should be minor. As a check, we compare the resulting stresses on the outer boundary (at  $r = R_0$ ) with the analytical expressions, which are given for  $\beta = 0$  in the following form:

$$\sigma_{11} + \sigma_{22} = \frac{|K|}{\sqrt{R_0}} \frac{1}{\sqrt{2\pi}} \left( e^{-i(\frac{\theta}{2} + \gamma)} + e^{i(\frac{\theta}{2} + \gamma)} \right), \quad (28a)$$

$$\sigma_{11} - \sigma_{22} + 2i\sigma_{12} = \frac{|K|}{\sqrt{R_0}} \frac{e^{i\theta}}{\sqrt{2\pi}} \left( e^{i(\frac{\theta}{2} + \gamma)} \cos \theta - e^{-i(\frac{\theta}{2} + \gamma)} \right). \quad (28b)$$

The individual stress components may be computed by extracting the real and imaginary components in (28), though we omit these expressions for brevity. In Fig. 6, we plot the analytical stress components as well as those computed from the finite element simulations, and we observe close agreement between the two.

We show example contour plots of the damage field  $d$  from the RVFTI simulations in Fig. 7, corresponding to the cases with  $\alpha = 0.25$  and  $\gamma = \pi/12$  and  $\pi/6$ . We also show how the kink angle  $\hat{\omega}$  is measured from the damage field. The final kink angles are presented in Fig. 5, alongside the theoretical predictions of He and Hutchinson (1989). Despite our use of a finite-radius notch and the subtle ambiguity of measuring kink angles from  $d$ , it can be seen that the kink angles compare reasonably well to the analytical values.

### 6.2.3. Crack trapping at the interface

We now consider the same semi-infinite crack at the bi-material interface, but we examine the conditions under which the crack would continue to grow along the interface, rather than kinking into material 2, see Fig. 8(a). In this situation, despite possible

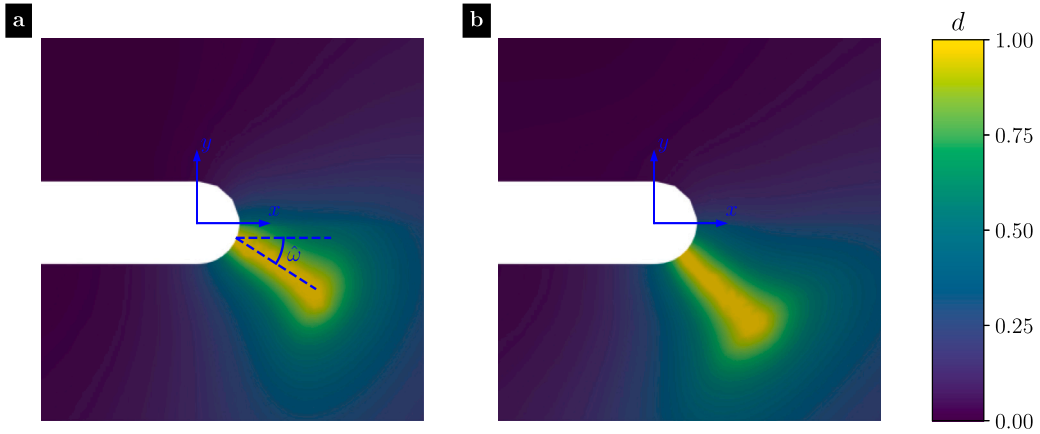


Fig. 7. Contour maps of the damage field computed using RVFTI for the crack at a bi-material interface. The simulations were for  $\alpha = 0.25$  and (a)  $\gamma = \pi/12$  and (b)  $\gamma = \pi/6$ . The crack set is taken where the material is fully-damaged,  $d = 1$ , and the kink angle  $\hat{\omega}$  is measured clockwise from the  $x$ -axis.

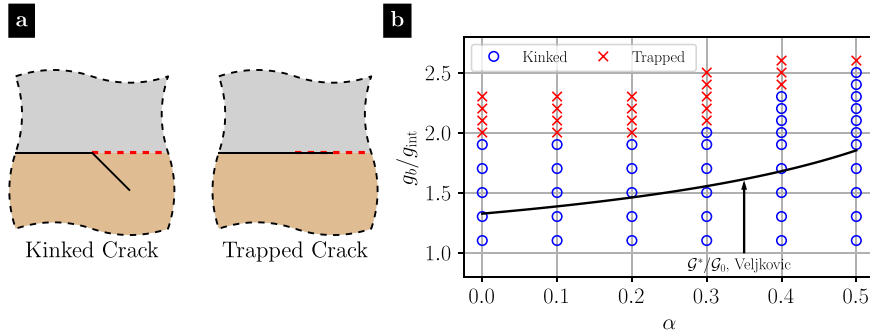


Fig. 8. Investigation of crack trapping at a bi-material interface. (a) Visual representation of crack kinking and crack trapping at a bi-material interface. (b) Simulation results using RVFTI for mode mixity  $\gamma = 3\pi/20$ , and varying the Dundurs mismatch parameter  $\alpha$  and the fracture toughness ratio  $g_b/g_{int}$ . Circles denote simulations where kinking out of the interface was observed, while crosses correspond to simulations where the crack remained trapped at the interface. The solid black curve shows the ratio  $G^*/G_0$ , computed using the approximations of Veljkovic (2005). From the theory of He and Hutchinson (1989), crack trapping is expected whenever  $g_b/g_{int} > G^*/G_0$  (above the black curve), while kinking occurs otherwise.

shear loading, the interface “traps” the crack. The possibility of crack trapping is considered in He and Hutchinson (1989), where the authors state that as long as the material fracture toughness ( $g_b$ ) is sufficiently larger than the interface fracture toughness ( $g_{int}$ ), the crack will remain trapped at the interface. The authors make the condition more precise: if  $\gamma$  is fixed, but the loading intensity is slowly increased, then by Griffith’s criterion and the condition of maximum energy release, the crack will grow in the first direction which reaches  $\mathcal{G}(\omega) = g(\omega)$ , where  $g(\omega)$  equals  $g_{int}$  when  $\omega = 0$  and  $g_b$  otherwise. From (25), there emerges two cases. First, if the crack were to kink into material 2, then  $G^* = \max_{\omega} \mathcal{G}(\omega) = g_b$ , while  $G_0 < g_{int}$ . In words, there exists a non-zero potential kink angle for which  $\mathcal{G}$  reaches the fracture toughness  $g_b$ , while there is insufficient driving force for the crack to continue along the interface. The second case is the opposite, wherein  $G_0 = g_{int}$ , but  $G^* < g_b$ . These two cases may be checked simultaneously by comparing the ratios  $G^*/G_0$  and  $g_b/g_{int}$ ; the kinking and trapping cases correspond to  $G^*/G_0 > g_b/g_{int}$  and  $G^*/G_0 < g_b/g_{int}$ , respectively.

We assess the prior condition using RVFTI. For these simulations, we use the same domain and boundary conditions as before; however we use a wider weak interface with  $m\epsilon = 2r_0 = R_0/1000$ . We also select  $k_\epsilon \in [10^{-6}, 10^{-3}]$ . We fix  $\gamma = 3\pi/20$  and vary  $\alpha \in [0, 0.5]$ . We choose  $g_i = 0.4$  N/mm, and we select  $g_b$  so that  $g_b/g_{int} \in [1, 2.6]$ , a range which encompasses the predicted values of  $G^*/G_0$ .

In Fig. 8(b), we show the results of our computations, indicating for which combinations of  $\alpha$  and  $g_b/g_{int}$  the crack is trapped versus kinks. Using the expressions of Veljkovic (2005) for the functions  $c(\omega, \alpha)$  and  $d(\omega, \alpha)$ , we also plot the variation of  $G^*/G_0$  with respect to  $\alpha$ . The points above (resp. below) this curve are those for which  $g_b/g_{int} > G^*/G_0$  (resp.  $g_b/g_{int} < G^*/G_0$ ), which indicates trapping (resp. kinking) according to the theory of He and Hutchinson (1989). We observe some quantitative disagreement between the simulations and theory. Notably, there are data points for which the crack kinks despite the theory predicting trapping. Nonetheless, there is qualitative agreement between the theoretical and computational boundaries between the trapping and kinking regimes.

## 7. Numerical simulations of toughness enhancement

In this section, we use RVFTI to investigate toughness enhancement in materials with weak interfaces. In particular, we study two-dimensional analogues of micro-architectural designs in SBs and ceramic composites to gain insights into the mechanisms which enhance toughness. Two specimens with specific micro-architectural designs are considered in this section:

- (1) a three-point bending in a multi-layered composite, where the bulk material has weak interfaces aligned perpendicular to the fracture growth direction, and
- (2) a single edge notch (SEN) geometry with a sinusoidal interface aligned with the crack growth direction.

### 7.1. Multi-layered specimen

The motivation to study multi-layered composites comes from the micro-architecture of spicules. As previously noted, spicules have a three-dimensional micro-architecture where the bulk material (mineral phase) is arranged in concentric layers separated by interfaces (organic phase).

Multi-layered geometries, which can be considered two-dimensional analogues of spicules, have been studied extensively in the context of ceramics (Clegg et al., 1990). Clegg et al. (1990) conducted experiments on SiC, which was made into thin sheets and coated with graphite forming weak interfaces. The sheets were then pressed together to form a layered micro-architecture which can be seen in Fig. 9(a.ii). The work of fracture for the layered SiC-graphite material, which was notched and tested under three point bending, was found to be  $4625 \text{ J/m}^2$ , while that of monolithic SiC was  $62 \text{ J/m}^2$ . As seen in Fig. 9(a.ii), the fracture surface of the layered material showed crack deflection into the weak interfaces. Meanwhile, the load–displacement response in Fig. 9(a.i) indicates that the ceramic composite did not catastrophically fail once the peak load was reached; rather, the material failed in a sequence of catastrophic steps beyond the peak load. From these experiments, it is unclear whether crack deflection was the only toughness-enhancing mechanism. Furthermore, any correlation between the crack path and the observed step-like features in the load–displacement response was not well investigated. We aim to address these points using RVFTI.

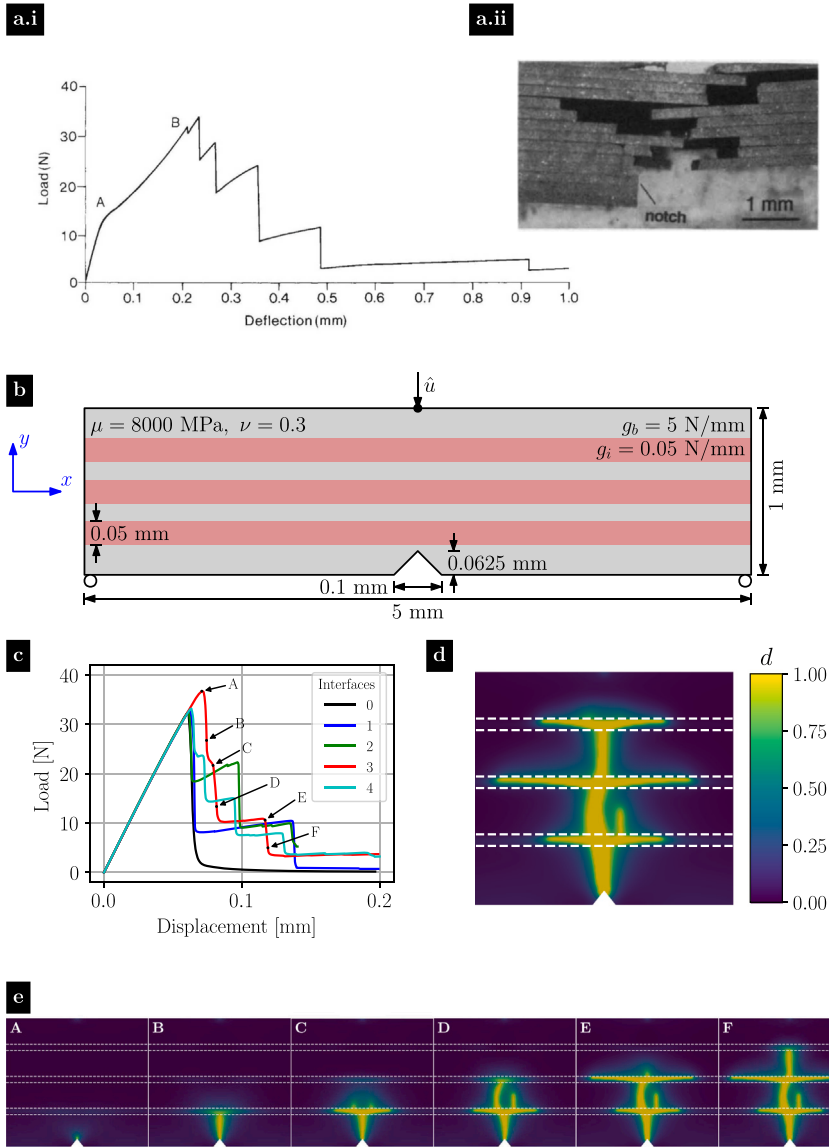
We consider the three-point bending specimen shown in Fig. 9(b), where the bulk material contains a number of weak interfaces that are aligned parallel to the span of the geometry. These interfaces are roughly uniformly-spaced along the vertical direction of the specimen. For the purpose of RVFTI, we take  $\varepsilon = 0.025 \text{ mm}$ , and we widen the interfaces to have total thickness  $2m\varepsilon = 0.05 \text{ mm}$ . We set  $k_\varepsilon \in [0, 5 \times 10^{-4}]$ . The bulk material has fracture toughness  $g_b = 0.5 \text{ N/mm}$ . Meanwhile, we select the fracture toughness in the widened interfaces to be  $g_i = 0.05 \text{ N/mm}$ , a factor of ten smaller than  $g_b$ . Via (8), the effective interface fracture toughness is around  $g_{\text{int}} \approx 0.125g_b$ . The V-notch is oriented perpendicular to the interfaces and the geometry is subjected to displacement-controlled three-point bending loads applied at the midpoint of the top surface. We note that the elastic properties are uniform throughout the composite (here, we take  $\mu = 8000 \text{ MPa}$  and  $\nu = 0.3$ ); only the toughness is varied in the widened interfaces.

Fig. 9(c) shows the effect of the number of layers on the load–displacement response. We observe that the geometry with zero interfaces (i.e., with uniform toughness  $g_b$ ) reaches a peak load and fails in a brittle manner, as shown by the almost vertical reduction in load after the peak is reached. However, in the specimen with one interface, the load–displacement curve shows a step-like feature after the peak load is reached similar to that seen by Clegg et al. (1990). We examine this further for the specimen with three interfaces, with the final crack path shown in Fig. 9(d). In Fig. 9(e), we show six stages of the evolution of the crack path, labeled A–F; the corresponding points in the load–displacement curve are indicated with black dots in Fig. 9(c). The peak load is reached at A, when the specimen fractures and grows up to the first weak interface at B. Between B and C, the crack deflects into the first weak interface. The crack then grows up to the second weak interface at D and is trapped in the second weak interface until E. Finally, the crack grows to the third interface at F, where it remains trapped until the simulation is terminated.

Observing the experimental and simulated load–displacement curves in Fig. 9, one might expect that the vertical sections of the curve would coincide with rapid crack growth in the bulk material, while the flat parts of the steps would correspond to stable crack growth within the weak interfaces. In contrast to our expectation, points B and D (when the crack first reaches an interface) are not at the bottom of the steps of the load–displacement curve. Rather, the load continues to drop even as the crack deflects into the interface. While this behavior may be an artifact of the simulation, the experiments of Clegg et al. (1990) do not use high-speed video recordings, and hence do not rule out the possibility of unstable growth of the deflected cracks within the weak layers. We believe this to be an interesting phenomenon which requires further experimental and numerical investigation.

We also remark that the load–displacement curve is flatter and longer on subsequent steps (between B–C and D–E, and beyond F). These features are also present in the load–displacement curve for SiC-graphite, Fig. 9(a.i). The increase in step flatness parallels the increase in system compliance as the crack grows. A possible interpretation for the increase in step length comes from beam bending theory. In beam bending theory, the maximum bending stress is proportional to both the applied displacement and the height of the beam. As the crack grows upward and deflects along a weak interface, the effective height of the beam decreases as the bottom layers of the beam are delaminated. Hence, if a vertical crack will nucleate when a critical stress is reached, then the necessary displacement must increase as the height is reduced. Finally, with respect to the remaining beam height, the thickness of a single layer represents an increasing fraction as the number of layers is reduced, thereby resulting in longer steps.

We lastly compute the work of fracture (i.e. the area under the load–displacement curves) for the multi-layered specimens. Respectively, for zero, one, two, three, and four interfaces the work of fracture is 1250, 1950, 2330, 2240, and  $2110 \text{ J/m}^2$ . The work of fracture increases from zero to two interfaces, but then decreases for three and four interfaces. This suggests that there may be an optimal number of interfaces for toughness enhancement, though further work is needed to understand how this number depends on design choices such as the material parameters, interface spacing, and specimen geometry.



**Fig. 9.** Toughening in a multi-layered specimen. (a.i) Load–deflection response of a SiC-graphite composite (Clegg et al., 1990). (a.ii) Final fracture surface in SiC-graphite composite (Clegg et al., 1990). (b) Geometry and loading of a micro-architecture with layers. The bulk material has fracture toughness  $g_b$ , while the widened interfaces are assigned fracture toughness  $g_i$ . The geometry has a V-notch and is subjected to three point bending loading conditions. (c) Load–displacement response for the layered micro-architecture specimen with zero to four interfaces. (d) Final crack path for the specimen with three interfaces. (e) Evolution of the crack path. The labels A–F in the panels of (e) coincide with the points of the load–displacement curve in (c).

## 7.2. Wavy interface

We demonstrated in the previous example how the presence of weak interfaces can enhance toughness via crack deflection and arrest. We next explore how the shape of the interface can also enhance toughness, which plays an important role in some SBs. For example, rams have wavy interfaces in their skull called suture joints that have been experimentally shown to enhance toughness (Jaslow, 1990). Suture joints which enhance toughness are also found in the beaks of woodpeckers (Lee et al., 2014). There have been experimental studies to determine the role of wavy, weak interfaces in enhancing toughness (Mirkhalaf et al., 2014; Lin et al., 2014), and several models have been used to understand this process (Zavattieri et al., 2007; Li et al., 2011, 2013). However, the role of other geometric factors, such as the amplitude of waviness, on toughness enhancement, is not well understood because the aforementioned models do not predict the crack path.

In this section, we review how interface geometry affects the toughness of the structure by computing the work of fracture for single edge notch (SEN) specimens with straight and wavy interfaces, depicted in Fig. 10(a). The notch has radius 0.01 mm and length 0.1 mm. For the wavy interface specimen, the interface is initially straight ahead of the notch so that the crack initiation load is identical to that of the straight interface specimen. After the straight portion, the wavy interface is sinusoidal with wavelength and amplitude  $\Lambda = A = 0.0625$  mm. The specimens have the same elastic parameters as the previous example,  $\mu = 8000$  MPa and  $\nu = 0.3$ . The bulk material has fracture toughness  $g_b = 0.5$  N/mm, and we select a wide-interface fracture toughness  $g_i = g_b/100$ . For RVFTI,  $\varepsilon = 0.004$  mm,  $k_\varepsilon = 5 \times 10^{-5}$ , and we widen the interfaces by an amount  $2m\varepsilon = 0.004$  mm. From these parameters, we compute  $g_{\text{int}} \approx 0.02g_b$ . The specimens are subjected to vertical displacement on the top surface of the domain.

The load–displacement response for both the specimens is shown in Fig. 10(b). The wavy interface specimen shows a higher work of fracture than the straight interface specimen. When the interface is straight, the crack propagates along the interface (see Fig. 10(c)). However, when the interface is wavy, the crack path becomes more complicated (see Fig. 10(d)).

Similar to the crack evolution in the multi-layered specimens, one might expect the crack to exhibit unstable growth between segments of the sinusoidal interface, followed by interludes of stable growth or trapping along the interface. However, the simulations show a more complicated behavior with three regimes. In Fig. 10(e), we show snapshots of a portion of the crack evolution as it grows between two segments of the weak interface corresponding to load steps A–E. The corresponding points in the load–displacement curve are shown in Fig. 10(b). From A to B, the crack is trapped along a segment of the weak interface. From B–C, the crack breaks out of the interface and grows in a stable fashion until the crack tip is roughly halfway between segments of the weak interface. From C–D, the crack growth becomes unstable and the crack rapidly grows to the next segment of the weak interface, where it is trapped until E and the cycle continues. This crack growth behavior is highly nontrivial, featuring growth along the interface and in the bulk material, as well as stable and unstable propagation, which highlights the ability of RVFTI to capture a wide variety of crack growth phenomena.

There are other interesting observations during the crack growth process. Cracks nucleate in the weak interface even before the main crack intersects it (see load step C in Fig. 10(e)). These daughter cracks form at the peaks and troughs of the weak interface and immediately ahead of the main crack. The effective interface fracture toughness is weaker than the bulk material (by approximately a factor of 1/50), so cracks nucleate due to the tensile stresses which are present ahead of main crack. This phenomenon is similar to the Cook-Gordon mechanism (Cook and Gordon, 1964), where the stress field of a crack approaching perpendicularly to a weak interface causes the nucleation of daughter cracks along said interface.

Lastly, like with the number of interfaces in the previous example, there is further room to explore how the amplitude  $A$  and wavelength  $\Lambda$  of the wavy interface can be chosen to optimize the work of fracture.

## 8. Discussion and conclusions

In this work, we presented a modified regularization of VFT to incorporate weak interfaces. Our goal was to model SBs, which are composites primarily made of a stiff mineral phase and interfaces composed of a compliant organic phase. In SBs, the interface thickness is several orders of magnitude smaller than that of the stiff mineral phase, and it is infeasible to resolve numerically across the interface. We note that our procedure may also be applied to problems with zero-thickness (atomically-thin) interfaces, such as grain boundaries or adhesive contact between dissimilar media.

In our modified regularization approach, we widened the weak interfaces by  $2m\varepsilon$ , where  $\varepsilon$  is the regularization length scale for VFT, and set the fracture toughness inside to a value  $g_i < g_b$ , where  $g_b$  is the fracture toughness of the surrounding material. In this way, the interfaces had reduced toughness, and the thickness of the interface decreased to 0 along with  $\varepsilon$ . We presented an analytical expression for the effective interface fracture toughness  $g_{\text{int}}$  in the limit of vanishing thickness of the interface, which depended on  $m$ ,  $g_b$ , and  $g_i$ . Notably, one was able to select  $m$  and  $g_i$  to achieve any desired value for the interface toughness  $g_{\text{int}}$ . We then proved a  $\Gamma$ -convergence result for two-dimensional domains with weak interfaces.

The regularization approach in this work is an important step towards modeling interface fracture and the complex crack patterns that form in SBs. In particular, we derived an effective fracture toughness for interfaces in a material with homogeneous  $g_b$ . In SBs such as spicules, the organic phase is mixed with the mineral phase, which may cause the fracture toughness  $g_b$  to vary within the mineral phase. Future work is needed to determine how the effective interface fracture toughness depends on local variation in  $g_b$ . Further, even under constant  $g_b$ , one may wish to model interfaces with varying toughness (i.e.  $g_{\text{int}}(x)$ ); it is interesting to explore whether the approach in this paper may accommodate such behavior, perhaps through appropriate selection of  $g_i$  or  $m$ .

We applied the modified regularization approach within a numerical implementation of VFT, which we termed RVFTI. While additional work is needed to connect the numerical model with the theory, we demonstrated that RVFTI reproduced the expected interface fracture toughness predicted by the theory. RVFTI was also used to study two toughening mechanisms in SBs due to the presence of layered microarchitectures and wavy interfaces. For the layered microarchitecture, we observed the “stepped” load–displacement curves present in experiments (Clegg et al., 1990), which corresponded in the simulations to crack arrest and deflection at the weak interfaces. Meanwhile, for the wavy interface specimen, bulk crack growth was impeded by both crack arrest and deflection, as well as the formation of daughter cracks. In both cases, more exhaustive parameter studies may be performed to explore which configurations achieve “optimal” toughness.

### CRedit authorship contribution statement

**Kaushik Vijaykumar:** Writing – original draft, Software, Methodology, Investigation. **Benjamin E. Grossman-Ponemon:** Writing – original draft, Methodology, Investigation, Formal analysis. **Yang Wan:** Software, Investigation. **Pooya Yousefi:** Formal analysis. **Christopher J. Larsen:** Methodology, Formal analysis. **Haneesh Kesari:** Writing – original draft, Supervision, Methodology, Research Design, Investigation, Conceptualization.



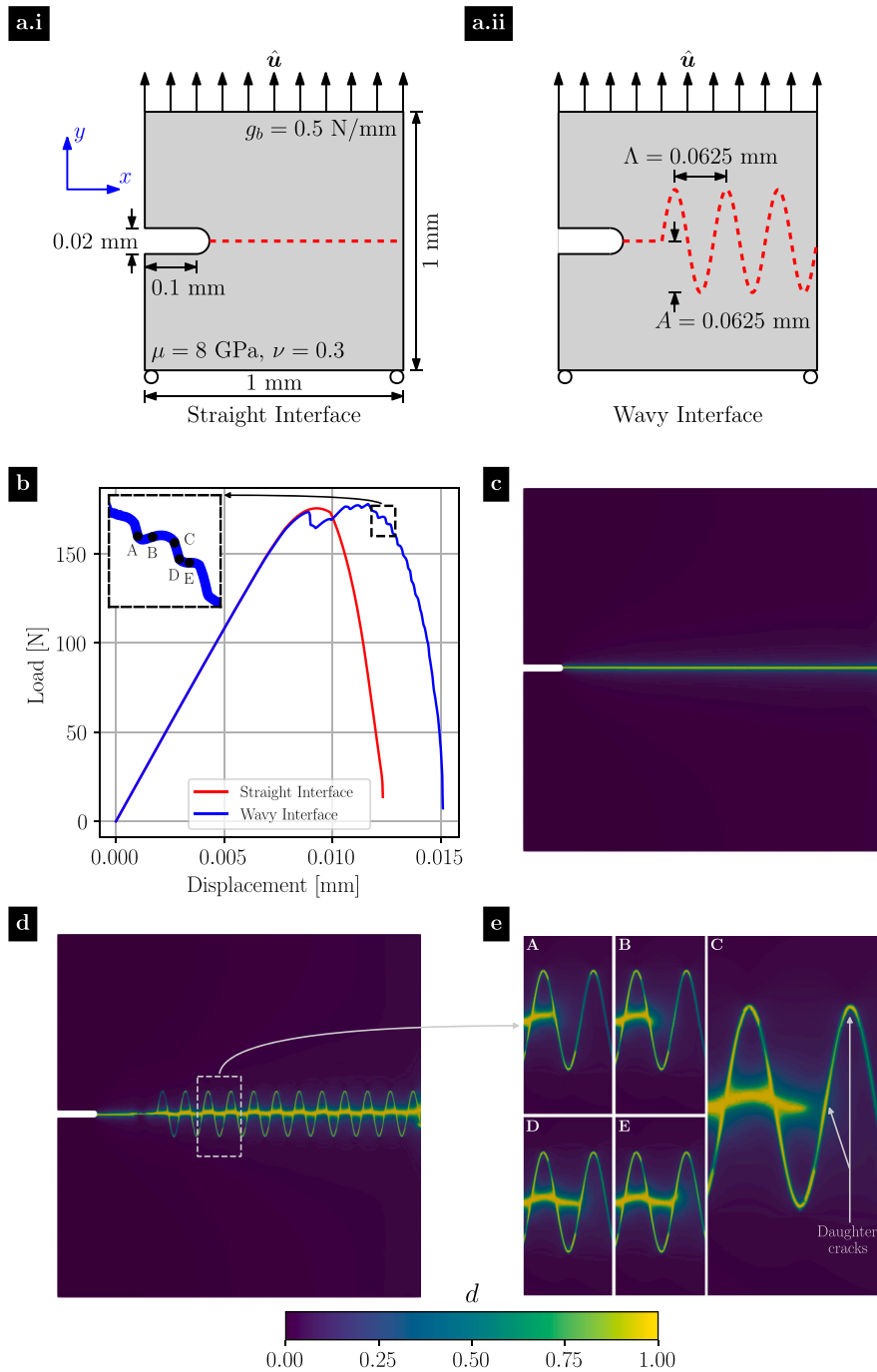


**Fig. 10.** The effect of interface shape on specimen toughness. (a) Geometry and loading for the (a.i) straight and (a.ii) wavy interface specimens. (b) Load–displacement curves for the two specimens. Step-like features are seen in the wavy interface specimen’s load–displacement response, see inset. (c) Final damage field for the straight interface specimen. (d) Final damage field for the wavy interface specimen. (e) Zoomed view for a portion of the damage field evolution in the wavy specimen. The labels A–E in subfigure (e) coincide with the black points in the load–displacement curve in subfigure (b).

**Declaration of competing interest**

The authors declare that they have no known competing financial interests or personal relationships that could have appeared to influence the work reported in this paper.

## Data availability

Data will be made available on request.

## Acknowledgments

Authors K.V., B.E.G.P., Y.W., and H.K. gratefully acknowledge the support of the U. S. Office of Naval Research (ONR) under PANTHER 1 N00014-18-1-2494, PANTHER 2 N00014-21-1-2044, PANTHER 3 N00014-21-1-2855, PANTHER 6 N0000003530, TIGER N00014-21-1-2054, and TIGER-2 N00014-23-1-2570 through Dr. Timothy Bentley. They also gratefully acknowledge the support of the U. S. Office of Naval Research under N00014-21-1-2815, and N00014-23-1-2688; and Collaborative Research Laboratory for Computational Materials Research at Brown University. Authors P.Y. and C.J.L. gratefully acknowledge the support of the U. S. National Science Foundation under grants DMS-1909991 and DMS-2206114.

## Appendix A. Additional mathematical results

**Proposition 5** (Properties of the Distance Function). *Let  $A \subset \mathbb{R}^n$  be a bounded domain. Then  $\text{dist}(x, A) : \mathbb{R}^n \rightarrow \mathbb{R}$  is a Lipschitz continuous function with Lipschitz constant 1. Moreover,  $\text{dist}(x, A) = \text{dist}(x, \bar{A})$ .*

### Proof.

1. Let  $y \in \mathbb{R}^n$ . Then  $\text{dist}(x, \{y\}) = |x - y| : \mathbb{R}^n \rightarrow \mathbb{R}$  is Lipschitz continuous with constant 1.

(a) For any  $x, z \in \mathbb{R}^n$ , we apply the reverse triangle inequality

$$\left| \text{dist}(x, \{y\}) - \text{dist}(z, \{y\}) \right| = \left| |x - y| - |z - y| \right| \leq |(x - y) - (z - y)| = |x - z|.$$

2. The function  $\text{dist}(x, \bar{A}) : \mathbb{R}^n \rightarrow \mathbb{R}$  is Lipschitz continuous with constant 1.

(a) Fix  $x \in \mathbb{R}^n$ . Via Step 1 the function  $\text{dist}(z, \{x\}) : \bar{A} \rightarrow \mathbb{R}$  is Lipschitz continuous over a compact set. Hence, it has a minimum, which it achieves at some point  $a \in \bar{A}$ . Thus,  $\text{dist}(x, \bar{A}) = |x - a|$ .

(b) Then, for any  $x, y \in \mathbb{R}^n$ :

$$\text{dist}(y, \bar{A}) - \text{dist}(x, \bar{A}) = \inf_{z \in \bar{A}} |y - z| - |x - a| \leq |y - a| - |x - a| \leq |y - x|,$$

where the last inequality results from the reverse triangle inequality.

(c) We may repeat item (a) for  $y$ ; we define its closest point in  $\bar{A}$  to be  $b$ . Then,

$$\text{dist}(x, \bar{A}) - \text{dist}(y, \bar{A}) = \inf_{z \in \bar{A}} |x - z| - |y - b| \leq |x - b| - |y - b| \leq |x - y|.$$

(d) Combining the two inequalities gives the desired conclusion.

$$\left| \text{dist}(x, \bar{A}) - \text{dist}(y, \bar{A}) \right| \leq |x - y|.$$

3. Finally, we prove  $\text{dist}(x, A) = \text{dist}(x, \bar{A})$ .

(a) For any  $x \in \mathbb{R}^n$ , let  $a \in \bar{A}$  be a closest point (i.e.  $\text{dist}(x, \bar{A}) = |x - a|$ ).

(b) There is a sequence  $(a_n)_n \subset A$  which converges to  $a$ .

(c) Because  $\bar{A} \supseteq A$ , we must have  $\text{dist}(x, \bar{A}) \leq \text{dist}(x, A)$ .

(d) For any  $n$ , we have

$$|x - a| = \text{dist}(x, \bar{A}) \leq \text{dist}(x, A) = \inf_{z \in A} |x - z| \leq |x - a_n| \leq |x - a| + |a - a_n|.$$

(e) Since  $|a - a_n|$  can be made arbitrarily small as  $n \rightarrow \infty$ , we have by the squeeze lemma

$$|x - a| \leq \text{dist}(x, A) \leq |x - a|.$$

which gives the conclusion.  $\square$

Here, we present some mathematical results related to the Hausdorff measure of curves and subsets of curves, which are used in the proofs in Section 4. The first result shows an equivalence between the Hausdorff measure and the arc length of a curve.

**Proposition 6** (Hausdorff Measure and Arc-Length). *Let  $\gamma : [a, b] \rightarrow \mathbb{R}^2$  be a continuous, injective, rectifiable curve with length  $L$ . Then, if  $\Gamma := \gamma([a, b])$ ,*

$$\mathcal{H}^1(\Gamma) = \mathcal{H}^1(\gamma([a, b])) = L.$$

**Proof.** The proof may be found in an equivalent result (Edgar, 2008, Theorem 6.3.8).  $\square$

The next result concerns the Hausdorff measure of subsets of curves.

**Proposition 7 (Hausdorff Measure of Subsets of Curves).** Let  $\gamma : [0, L] \rightarrow \mathbb{R}^2$  be an injective,  $C^1$ -continuous function such that  $|\gamma'(s)| = 1$  for almost every  $s \in [0, L]$ . This is an arc-length parameterization of the curve  $\gamma([0, L])$ . Then, for any  $A \subseteq [0, L]$ ,

$$\mathcal{H}^1(\gamma(A)) = \mathcal{L}^1(A).$$

**Proof.**

1. We recapitulate (Evans and Gariepy, 2015, Theorem 1.8). For any Radon measure  $\mu$  (such as the Lebesgue measure),

$$\mu(A) = \inf\{\mu(U) : A \subseteq U, U \text{ open}\}.$$

2. Any open set  $U \subset \mathbb{R}$  may be written as a countable union of pairwise-disjoint open intervals  $(I_k)_k$ .
3. Combining Steps 1 and 2,

$$\mathcal{L}^1(A) = \inf\left\{\sum_{k=1}^{\infty} \mathcal{L}^1(I_k) : A \subseteq \bigcup_{k=1}^{\infty} I_k, I_k \text{ pairwise-disjoint}\right\}.$$

Without issue, we may restrict these sets to lie within the interval  $[0, L]$  (i.e. redefine  $I_k \leftarrow I_k \cap [0, L]$ ).

4. Next, let us take an infimizing sequence of open sets  $(U_j)_j$ . Then, we have

$$\mathcal{L}^1(U_j) \rightarrow \mathcal{L}^1(A).$$

Moreover,  $\mathcal{L}^1(U_j \setminus A) \rightarrow 0$ .

5. By Evans and Gariepy (2015, Theorem 2.8), we have

$$\mathcal{H}^1(\gamma(U_j \setminus A)) \leq Lip(\gamma)\mathcal{L}^1(U_j \setminus A) \rightarrow 0,$$

where  $Lip(\gamma)$  is the Lipschitz constant for  $\gamma$  (here equal to 1). This means

$$\mathcal{H}^1(\gamma(U_j)) \rightarrow \mathcal{H}^1(\gamma(A)).$$

Moreover, applying Proposition 6 to each pairwise-disjoint interval  $I_{jk}$  in  $U_j$ ,

$$\mathcal{H}^1(\gamma(U_j)) = \sum_{k=1}^{\infty} \mathcal{H}^1(\gamma(I_{jk})) = \sum_{k=1}^{\infty} \mathcal{L}^1(I_{jk}) = \mathcal{L}^1(U_j).$$

Hence, taking the limit as  $j \rightarrow \infty$  of both sides, we reach the conclusion

$$\mathcal{H}^1(\gamma(A)) = \mathcal{L}^1(A). \quad \square$$

The final result concerns covering closed subsets of a rectifiable curve by a finite number of pairwise disjoint, closed, simply-connected subsets.

**Proposition 8.** Let  $\gamma : [0, L] \rightarrow \mathbb{R}^2$  be as in Proposition 7, and let  $A \subset \gamma([0, L])$  be closed or  $\mathcal{H}^1$ -almost closed (i.e.  $\mathcal{H}^1(\overline{A}/A) = 0$ ). Then, for any  $\eta > 0$ , there exists a finite cover of  $\overline{A}$  by pairwise disjoint sets  $(A_i)_{i=1}^{N_\eta}$  such that each  $A_i$  is the image of  $[a_i, b_i] \subseteq [0, L]$  under  $\gamma$ , and

$$\mathcal{H}^1(A) = \mathcal{H}^1(\overline{A}) \leq \mathcal{H}^1\left(\bigcup_{i=1}^{N_\eta} A_i\right) = \sum_{i=1}^{N_\eta} \mathcal{H}^1(A_i) < \mathcal{H}^1(A) + \eta.$$

**Proof.**

1. If  $A$  is  $\mathcal{H}^1$ -almost closed, then  $\mathcal{H}^1(\overline{A}) = \mathcal{H}^1(A)$ , and so the result is unchanged. Going forward, we assume  $A$  is closed.
2. Let  $B := \gamma_i^{-1}(A)$ . By Proposition 7, we have

$$\mathcal{H}^1(A) = \mathcal{L}^1(B).$$

3. Because  $\gamma$  is a continuous function and  $A$  is closed,  $B$  must also be closed.
4. As in the proof of Proposition 7, for any  $\eta > 0$ , we may find an open set  $U \supset B$  such that

$$\mathcal{L}^1(U) = \mathcal{L}^1(B) + \eta.$$

Again, this is an open subset of  $\mathbb{R}$ , and hence can be expressed as a countable union of pairwise-disjoint open intervals  $(U_i)_{i=1}^{\infty}$ . Again, without issue, we may restrict these sets to the domain  $[0, L]$  (the domain of  $\gamma$ ).

5. The set  $(U_i)_{i=1}^\infty$  is a cover of  $B$ . Meanwhile,  $B$  is a closed and bounded subset of  $\mathbb{R}$ , and hence is compact. Thus, there exists a finite subcover consisting of pairwise-disjoint open intervals  $(U_i)_{i=1}^{M_\eta}$  (we have not relabeled in  $i$ ) such that

$$B \subset \bigcup_{i=1}^{M_\eta} U_i$$

and hence

$$\mathcal{L}^1(B) \leq \sum_{i=1}^{M_\eta} \mathcal{L}^1(U_i) < \sum_{i=1}^\infty \mathcal{L}^1(U_i) = \mathcal{L}^1(U) = \mathcal{L}^1(B) + \varepsilon.$$

6. For each  $i$ , we may write  $U_i = (a_i, b_i)$ , and  $\overline{U_i} = [a_i, b_i]$ . We have  $\mathcal{L}^1(\overline{U_i}) = \mathcal{L}^1(U_i) = b_i - a_i$ .  
 7. For any  $i \neq j$ , if  $\overline{U_i} \cap \overline{U_j} \neq \emptyset$ , then these sets must overlap at one of the endpoints (since the open sets are disjoint). Hence, we can define  $\overline{V_i} = \overline{U_i} \cup \overline{U_j} = [\min(a_i, a_j), \max(b_i, b_j)]$ , and we have  $\mathcal{L}^1(\overline{V_i}) = \mathcal{L}^1(\overline{U_i}) + \mathcal{L}^1(\overline{U_j}) = \max(b_i, b_j) - \min(a_i, a_j)$ . Repeating this way, we end up with a finite set  $(V_i)_{i=1}^{N_\eta}$  of closed, pairwise disjoint intervals (with  $N_\eta \leq M_\eta$ ) such that

$$\sum_{i=1}^{N_\eta} \mathcal{L}^1(V_i) = \sum_{j=1}^{M_\eta} \mathcal{L}^1(\overline{U_j}) = \sum_{j=1}^{M_\eta} \mathcal{L}^1(U_j) < \mathcal{L}^1(B) + \eta.$$

8. Set  $A_i := \gamma(V_i)$ . Then

$$A \subset \bigcup_{i=1}^{N_\eta} A_i.$$

We remark that since the closed intervals  $(V_i)_i$  are pairwise disjoint, then so too must be the sets  $(A_i)_i$ . Thus,

$$\mathcal{H}^1(A) \leq \mathcal{H}^1\left(\bigcup_{i=1}^{N_\eta} A_i\right) = \sum_{i=1}^{N_\eta} \mathcal{H}^1(A_i).$$

9. Finally, by Proposition 7,

$$\mathcal{H}^1(A) \leq \sum_{i=1}^{N_\eta} \mathcal{H}^1(A_i) = \sum_{i=1}^{N_\eta} \mathcal{L}^1(V_i) < \mathcal{L}^1(B) + \eta = \mathcal{H}^1(A) + \eta. \quad \square$$

### Appendix B. Proof of preliminary results

Here, we present the proofs for the preliminary results in Sections 4.3 and 4.4.

#### Proof of Proposition 2.

1. As the composition of two continuous functions (the distance function to  $J_i$  and  $\gamma_i$ ), the function  $\text{dist}(\gamma_i(\cdot), J_i) : [0, \mathcal{H}^1(I_i)] \rightarrow \mathbb{R}$  is also continuous. Moreover, it is defined over the compact set  $[0, \mathcal{H}^1(I_i)]$  and so it achieves its maximum.
2. By assumption on  $I$  (cf. Section 4.1), an interface curve only intersects other interface curves (or the domain boundary) at its endpoints. Hence,  $\max_{s \in [0, \mathcal{H}^1(I_i)]} \text{dist}(\gamma_i(s), J_i) > 0$ . Thus,

$$\{s \in [0, \mathcal{H}^1(I_i)] : \text{dist}(\gamma_i(s), J_i) > 3\rho\}$$

is nonempty whenever  $3\rho < \max_{s \in [0, \mathcal{H}^1(I_i)]} \text{dist}(\gamma_i(s), J_i)$ ; hence  $A_{i\rho}$  is also nonempty.

3. We prove Property 1 in the Proposition. For this step, let  $\mathbf{x} \in A_{i\rho}$ .

(a) Let  $\mathbf{y} \in I_j$  for  $j \neq i$ . Suppose  $\ell_{i\rho} \cap \ell_{i\rho} \neq \emptyset$ , and let  $\mathbf{z} \in \ell_{i\rho} \cap \ell_{i\rho}$ . Then, via the triangle inequality

$$|\mathbf{x} - \mathbf{y}| \leq |\mathbf{x} - \mathbf{z}| + |\mathbf{z} - \mathbf{y}| \leq 2\rho.$$

However,  $\mathbf{y} \in J_j$ , and so

$$|\mathbf{x} - \mathbf{y}| \geq \text{dist}(\mathbf{x}, J_j) > 3\rho,$$

which yields the contradiction  $3\rho < 2\rho$ . Hence,  $\ell_{i\rho} \cap \ell_{i\rho} = \emptyset$ .

(b) A similar sequence of steps may be used to show that  $\ell_{i\rho} \cap \partial B = \emptyset$ .

(c) Let  $\mathbf{y} \in I_i$  with  $\mathbf{x} \neq \mathbf{y}$ . Suppose  $\ell_{i\rho} \cap \ell_{i\rho} \neq \emptyset$ , and let  $\mathbf{z} \in \ell_{i\rho} \cap \ell_{i\rho}$ . Under the coordinate map (11), we have

$$\mathbf{z} = \gamma_i(s_x) + |\mathbf{z} - \mathbf{x}| \hat{\mathbf{n}}_i(s_x) = \gamma_i(s_y) + |\mathbf{z} - \mathbf{y}| \hat{\mathbf{n}}_i(s_y)$$

where  $s_x = \gamma_i^{-1}(\mathbf{x})$  and  $s_y = \gamma_i^{-1}(\mathbf{y})$ . However, since  $s_x \neq s_y$  and  $|\mathbf{z} - \mathbf{x}|, |\mathbf{z} - \mathbf{y}| < \rho < \rho_i$ , this implies that the coordinate map is not injective, which contradicts the existence of the tubular neighborhood. Hence,  $\ell_{i\rho} \cap \ell_{i\rho} = \emptyset$ .

4. We next prove Property 2 in the Proposition. Let  $y \in \ell_{ix\rho}$  for some  $x \in A_{i\rho}$ . Because  $\cup_{j \neq i} I_j \subset J_i$ ,  $\text{dist}(y, \cup_{j \neq i} I_j) \geq \text{dist}(y, J_i) > \text{dist}(x, J_i) - |y - x| > 2\rho$ . Meanwhile  $\text{dist}(y, I_i) < |y - x| < \rho$ , and so we must have

$$\text{dist}(y, I) = \text{dist}(y, I_i).$$

Next, suppose there exists  $z \in I_i$  (with  $z \neq x$ ) such that  $\text{dist}(y, I_i) = |y - z|$ . From the previous argument, we know  $z \notin \{\gamma_i(0), \gamma_i(\mathcal{H}^1(I_i))\} \subset J_i$ . Hence,  $\gamma_i^{-1}(z) =: s_z \in (0, \mathcal{H}^1(I_i))$ . As a minimizer of the distance function in the interior of the interval  $[0, \mathcal{H}^1(I_i)]$ ,  $s_z$  must also be a stationary point of the function  $|y - \gamma_i(s)|^2/2$ . However, this means that

$$(y - \gamma_i(s_z)) \cdot \gamma_i'(s_z) = (y - z) \cdot \hat{t}_i(s_z) = 0.$$

Thus,  $y \in \ell_{iz\rho}$  or  $\ell_{ix\rho} \cap \ell_{iz\rho} \neq \emptyset$ , which contradicts 1. Hence,  $z = x$ , and so

$$\text{dist}(y, I_i) = |y - x|.$$

5. Finally, we prove Property 3 in the Proposition.

(a) We may show

$$I_i \setminus A_{i\rho} = \gamma_i(\{s \in [0, \mathcal{H}^1(I_i)] : \text{dist}(\gamma_i(s), J_i) \leq 3\rho\}).$$

(b) Applying Proposition 7,

$$\mathcal{H}^1(I_i \setminus A_{i\rho}) = \mathcal{L}^1(\{s \in [0, \mathcal{H}^1(I_i)] : \text{dist}(\gamma_i(s), J_i) \leq 3\rho\}).$$

(c) Via continuity of measures on nesting sets,

$$\begin{aligned} \lim_{\rho \rightarrow 0+} \mathcal{L}^1(\{s \in [0, \mathcal{H}^1(I_i)] : \text{dist}(\gamma_i(s), J_i) \leq 3\rho\}) &= \mathcal{L}^1\left(\bigcap_{\rho > 0} \{s \in [0, \mathcal{H}^1(I_i)] : \text{dist}(\gamma_i(s), J_i) \leq 3\rho\}\right) \\ &= \mathcal{L}^1(\{s \in [0, \mathcal{H}^1(I_i)] : \text{dist}(\gamma_i(s), J_i) = 0\}). \end{aligned}$$

(d) By construction of  $I$ , the interface curve  $I_i$  may only intersect another interface curve  $I_j$  or the domain boundary at its endpoints. Hence

$$\{s \in [0, \mathcal{H}^1(I_i)] : \text{dist}(\gamma_i(s), J_i) = 0\} = \{0, \mathcal{H}^1(I_i)\},$$

which is a set with only two elements, and so

$$\mathcal{L}^1(\{s \in [0, \mathcal{H}^1(I_i)] : \text{dist}(\gamma_i(s), J_i) = 0\}) = 0.$$

(e) Hence,

$$\lim_{\rho \rightarrow 0+} \mathcal{H}^1(I_i \setminus A_{i\rho}) = 0.$$

(f) Finally,

$$\mathcal{H}^1(\Gamma \cap A_{i\rho}) = \mathcal{H}^1(\Gamma \cap I_i) - \mathcal{H}^1(\Gamma \cap (I_i \setminus A_{i\rho})).$$

Because  $\mathcal{H}^1(\Gamma \cap (I_i \setminus A_{i\rho})) \leq \mathcal{H}^1(I_i \setminus A_{i\rho})$ , which shrinks to zero as  $\rho \rightarrow 0+$ , we have

$$\lim_{\rho \rightarrow 0+} \mathcal{H}^1(\Gamma \cap A_{i\rho}) = \mathcal{H}^1(\Gamma \cap I_i). \quad \square$$

We next prove Proposition 3. Our proof strategy mirrors existing proof strategies for  $\Gamma$ -lim inf results for domains with homogeneous fracture toughness  $g$ , for example (Braidès, 2002, Theorem 8.1).

**Proof of Proposition 3.**

1. Let us denote the functional in (15a) as  $\overline{\Pi}_{\varepsilon_n}$ . Without loss of generality, we may assume that  $\liminf_{n \rightarrow \infty} \overline{\Pi}_{\varepsilon_n}[u_n, d_n] < \infty$ . Otherwise, the result is trivial to show.

2. Take a subsequence  $(u_{n_k}, d_{n_k})_k$  of  $(u_n, d_n)_n$  so that

$$\lim_{k \rightarrow \infty} \overline{\Pi}_{\varepsilon_n}[u_{n_k}, d_{n_k}] = \liminf_{n \rightarrow \infty} \overline{\Pi}_{\varepsilon_n}[u_n, d_n].$$

Going forward, we abuse notation by referring to the subsequence as  $(u_n, d_n)_n$ .

3. Because  $\lim_{n \rightarrow \infty} \overline{\Pi}_{\varepsilon_n}[u_n, d_n] < \infty$ , then there must be a constant  $M < \infty$  such that  $\overline{\Pi}_{\varepsilon_n}[u_n, d_n] < M$ . In particular, the same bound holds for the elastic energy:

$$0 \leq \int_{-\rho}^{\rho} (1 - d_n)^2 C(u_n')^2 dz \leq M < \infty.$$

4. Via the Sobolev Embedding Theorem (Adams and Fournier, 2003),  $H^1((-\rho, \rho); \mathbb{R}) \hookrightarrow C^0([-\rho, \rho]; \mathbb{R})$ , so that  $u_n$  and  $d_n$  have continuous representatives in their equivalence classes. In particular, these representative functions are bounded on  $[-\rho, \rho]$ . Going forward, where it is necessary we will abuse notation and let  $u_n$  and  $d_n$  to refer to the continuous representatives in the original equivalence classes.
5. Pick  $0 < \delta < \rho$ . Using the uniform bound for the elastic energy and the continuity (and boundedness) of the function  $(1 - d_n)^2$ , we trivially have

$$M \geq \int_{-\delta}^{\delta} (1 - d_n)^2 C(u'_n)^2 dz \geq C \min_{[-\delta, \delta]} (1 - d_n)^2 \int_{-\delta}^{\delta} (u'_n)^2 dz.$$

6. Take a subsequence  $(u_{n_k}, d_{n_k})_k$  of  $(u_n, d_n)_n$  such that

$$\lim_{k \rightarrow \infty} \left( \min_{[-\delta, \delta]} (1 - d_{n_k})^2 \right) = \liminf_{n \rightarrow \infty} \left( \min_{[-\delta, \delta]} (1 - d_n)^2 \right)$$

and define this limit to be  $m_\delta$ , which must be non-negative. As before, we abuse notation by referring to the new subsequence as  $(u_n, d_n)_n$ .

7. Suppose  $m_\delta > 0$ . There must exist an index  $N$  such that, for all  $n > N$ , we have

$$\min_{[-\delta, \delta]} (1 - d_n)^2 > m_\delta/2.$$

This implies

$$\int_{-\delta}^{\delta} (u'_n)^2 dz \leq \max \left\{ \max_{1 \leq k \leq N} \int_{-\delta}^{\delta} (u'_k)^2 dz, \frac{2M}{Cm_\delta} \right\},$$

or that  $(u'_n)_n$  is a bounded sequence in  $L^2((-\delta, \delta); \mathbb{R})$ . By weak compactness in  $L^2((-\delta, \delta); \mathbb{R})$  (Evans and Gariepy, 2015, Theorem 1.42), there is a subsequence  $(u'_{n_k})_k$  of  $(u'_n)_n$  such that  $u'_{n_k} \rightharpoonup f \in L^2((-\delta, \delta); \mathbb{R})$  as  $k \rightarrow \infty$ . That is, for any  $v \in L^2((-\delta, \delta); \mathbb{R})$ , we have

$$\int_{-\delta}^{\delta} u'_{n_k} v dz \rightarrow \int_{-\delta}^{\delta} f v dz.$$

If we restrict our attention to  $v \in C_c^\infty((-\delta, \delta); \mathbb{R})$ , then applying integration by parts gives

$$\int_{-\delta}^{\delta} u'_{n_k} v dz = - \int_{-\delta}^{\delta} u_{n_k} v' dz.$$

Using strong convergence of  $u_{n_k}$  to  $u$  in  $L^2((-\delta, \delta); \mathbb{R})$ , we also have

$$- \int_{-\delta}^{\delta} u_{n_k} v' dz \rightarrow - \int_{-\delta}^{\delta} u v' dz.$$

If we combine the weak convergence of  $u'_{n_k}$  to  $f$  and the strong convergence of  $u_{n_k}$  to  $u$ , we arrive at

$$\int_{-\delta}^{\delta} f v dz = - \int_{-\delta}^{\delta} u v' dz,$$

which holds for any  $v \in C_c^\infty((-\delta, \delta); \mathbb{R})$ . However, the previous equation is precisely the definition of the weak derivative of  $u$ , which implies that  $u \in H^1((-\delta, \delta); \mathbb{R})$ . This contradicts the assumptions on  $u$  in the proposition statement.

8. Hence,

$$\lim_{n \rightarrow \infty} \left( \min_{[-\delta, \delta]} (1 - d_n)^2 \right) = 0.$$

Thus, there must exist  $(z_n)_n \subset [-\delta, \delta]$  so that  $d_n(z_n) \rightarrow 1$ .

9. For each  $n$ , define

$$\mathcal{V}_n = \{d \in H^1((-\rho, \rho); \mathbb{R}) : d(z_n) = d_n(z_n)\}.$$

We have

$$\overline{\Pi}_{\varepsilon_n}(u_n, d_n) \geq \int_{-\rho}^{\rho} \frac{\overline{g}(z/\varepsilon_n)}{2} \left( \frac{d^2}{\varepsilon_n} + \varepsilon_n (d')^2 \right) dz \geq \inf_{d \in \mathcal{V}_n} \int_{-\rho}^{\rho} \frac{\overline{g}(z/\varepsilon_n)}{2} \left( \frac{d^2}{\varepsilon_n} + \varepsilon_n (d')^2 \right) dz.$$

10. Any  $d \in \mathcal{V}_n$  may be written as  $d = d_n(z_n) \tilde{d}$ , where  $\tilde{d} \in \tilde{\mathcal{V}}_n = \{d \in H^1((-\rho, \rho); \mathbb{R}) : d(z_n) = 1\}$ . Moreover,

$$\inf_{d \in \mathcal{V}_n} \int_{-\rho}^{\rho} \frac{\overline{g}(z/\varepsilon_n)}{2} \left( \frac{d^2}{\varepsilon_n} + \varepsilon_n (d')^2 \right) dz = (d_n(z_n))^2 \inf_{\tilde{d} \in \tilde{\mathcal{V}}_n} \int_{-\rho}^{\rho} \frac{\overline{g}(z/\varepsilon_n)}{2} \left( \frac{\tilde{d}^2}{\varepsilon_n} + \varepsilon_n (\tilde{d}')^2 \right) dz.$$

11. As a shorthand, let us define  $f(\varepsilon_n, z_n, \rho)$  to be the infimum on the right hand side of the previous equation. From the Euler-Lagrange equations, one may directly compute  $f(\varepsilon_n, \cdot, \rho)$  and show that it is continuous on  $[-\delta, \delta]$  and hence admits a minimum. Then,

$$\overline{\Pi}_{\varepsilon_n}(u_n, d_n) \geq (d_n(z_n))^2 f(\varepsilon_n, z_n, \rho) \geq (d_n(z_n))^2 \min_{z \in [-\delta, \delta]} f(\varepsilon_n, z, \rho).$$

12. We take the limits of both sides of the previous equation as  $n \rightarrow \infty$ :

$$\lim_{n \rightarrow \infty} \overline{\Pi}_{\varepsilon_n}(u_n, d_n) \geq \lim_{n \rightarrow \infty} \left( (d_n(z_n))^2 \min_{z \in [-\delta, \delta]} f(\varepsilon_n, z, \rho) \right).$$

Via Step 8, we have that  $\lim_{n \rightarrow \infty} d_n(z_n) = 1$ . We may show that

$$\lim_{n \rightarrow \infty} \left( \min_{z \in [-\delta, \delta]} f(\varepsilon_n, z, \rho) \right) = g_{\text{int}}.$$

Combining these limits, and recalling that the subsequences were chosen in Step 2 and Step 6 so that  $\lim_{n \rightarrow \infty} \overline{\Pi}_{\varepsilon_n}(u_n, d_n)$  is precisely the original limit inferior in (15a), we reach the desired conclusion.  $\square$

Finally, we prove Proposition 4.

**Proof of Proposition 4.**

- Let  $A := \gamma_i([s_0, s_1])$ . We claim that  $\partial \mathcal{N}_\rho(A)$  is a subset of the union of four sets: the boundaries of  $\rho$ -neighborhoods of  $\gamma_i(s_0)$  and  $\gamma_i(s_1)$  (i.e. circles with radius  $\rho$  about the two endpoints) and the images of  $[s_0, s_1]$  under the maps

$$y_\pm(s) = \gamma_i(s) \pm \rho \hat{n}_i(s).$$

Proof of the claim:

- For any  $x \in \partial \mathcal{N}_\rho(A)$ , let the closest point projection onto  $A$  be  $\pi_A(x)$ . We note that this may not be unique depending on the value of  $\rho$ . Let  $s = \gamma_i^{-1}(\pi_A(x))$ .
- If  $s = s_0$  or  $s_1$ , then we trivially have that  $x \in \partial \mathcal{N}_\rho(\gamma_i(s_0))$  or  $\partial \mathcal{N}_\rho(\gamma_i(s_1))$ .
- If  $s \in (s_0, s_1)$ , then  $x - \gamma_i(s)$  must be orthogonal to  $\hat{t}_i(s)$ . Hence, it can be written as  $\gamma_i(s) \pm \rho \hat{n}_i(s)$ .

We next bound the length of each of the four sets.

- Each circle has circumference  $2\pi\rho$ .
- Meanwhile, the arc lengths of the other two sets are computed using

$$\int_{s_0}^{s_1} |y'_\pm(s)| \, ds.$$

We may directly compute the derivatives of  $y_\pm$ :<sup>11</sup>

$$y'_\pm(s) = \left( 1 \pm \frac{\rho}{R_i(s)} \right) \hat{t}_i(s).$$

Thus,

$$\int_{s_0}^{s_1} |y'_\pm(s)| \, ds = \int_{s_0}^{s_1} \left| 1 \pm \frac{\rho}{R_i(s)} \right| \, ds \leq \int_{s_0}^{s_1} \left( 1 + \frac{\rho}{R_{\min}} \right) \, ds \leq \left( 1 + \frac{\rho}{R_{\min}} \right) (s_1 - s_0).$$

- Since  $s_1 - s_0 = H^1(A)$ , we can put together the estimates for the four pieces to yield the conclusion.  $\square$

**References**

Abaqus, 2012. Reference Manual.  
 Abate, M., Tovena, F., 2012. Curves and Surfaces. In: UNITEXT, Springer-Verlag, Milan.  
 Adams, R.A., Fournier, J.J., 2003. Sobolev Spaces. In: Pure and Applied Mathematics, vol. 140, Academic Press.  
 Ambati, M., Gerasimov, T., De Lorenzis, L., 2015. A review on phase-field models of brittle fracture and a new fast hybrid formulation. *Comput. Mech.* 55 (2), 383–405.  
 Ambrosio, L., Coscia, A., Dal Maso, G., 1997. Fine properties of functions with bounded deformation. *Arch. Ration. Mech. Anal.* 139 (3), 201–238.  
 Ambrosio, L., Fusco, N., Pallara, D., 2000. Functions of Bounded Variation and Free Discontinuity Problems. Clarendon Press, Oxford.  
 Ambrosio, L., Tortorelli, V.M., 1990. Approximation of functionals depending on jumps by elliptic functional via  $\Gamma$ -convergence. *Comm. Pure Appl. Math.* 43 (8), 999–1036.  
 Ambrosio, L., Tortorelli, V.M., 1992. On the approximation of free discontinuity problems. *Boll. Unione Mat. Ital.* B 7 (6), 105–123.  
 Anderson, P.M., 1988. Small scale contact conditions for the linear-elastic interface crack. *J. Appl. Mech.* 55 (4), 814–817.  
 Anderson, T.L., 2005. Fracture Mechanics: Fundamentals and Applications. CRC Press.  
 Barthelat, F., Espinosa, H., 2007. An experimental investigation of deformation and fracture of nacre–mother of pearl. *Exp. Mech.* 47 (3), 311–324.  
 Barthelat, F., Rabiee, R., 2011. Toughness amplification in natural composites. *J. Mech. Phys. Solids* 59 (4), 829–840.  
 Borden, M.J., Verhoosel, C.V., Scott, M.A., Hughes, T.J., Landis, C.M., 2012. A phase-field description of dynamic brittle fracture. *Comput. Methods Appl. Mech. Engrg.* 217, 77–95.  
 Bourdin, B., Francfort, G.A., Marigo, J.-J., 2000. Numerical experiments in revisited brittle fracture. *J. Mech. Phys. Solids* 48 (4), 797–826.  
 Bourdin, B., Francfort, G.A., Marigo, J.-J., 2008. The variational approach to fracture. *J. Elasticity* 91 (1–3), 5–148.  
 Bower, A., Ortiz, M., 1991. A three-dimensional analysis of crack trapping and bridging by tough particles. *J. Mech. Phys. Solids* 39 (6), 815–858.

<sup>11</sup> This follows from the fact that  $\hat{n}_i(s) = Q^T \hat{i}_i(s) = Q^T \gamma'_i(s)$ . Hence  $\hat{n}'_i(s) = Q \gamma''_i(s)$ , which we note must be orthogonal to  $\hat{n}_i(s)$ . Finally,  $\hat{t}_i(s) \cdot \hat{n}'_i(s) = \hat{t}_i(s) \cdot (Q \gamma''_i(s)) = (Q^T \hat{t}_i(s)) \cdot \gamma''_i(s) = -\hat{n}_i(s) \cdot \gamma''_i(s) = 1/R_i(s)$ , where  $Q^T$  is the transpose of the orthogonal transformation  $Q$ .

- Brach, S., Hossain, M., Bourdin, B., Bhattacharya, K., 2019. Anisotropy of the effective toughness of layered media. *J. Mech. Phys. Solids* 131, 96–111. <http://dx.doi.org/10.1016/j.jmps.2019.06.021>.
- Braides, A., 2002.  $\Gamma$ -Convergence for Beginners. In: *Oxford Lecture Series in Mathematics and its Applications*, vol. 22, Oxford University Press.
- Brodnik, N.R., Brach, S., Long, C.M., Ravichandran, G., Bourdin, B., Faber, K.T., Bhattacharya, K., 2021. Fracture diodes: Directional asymmetry of fracture toughness. *Phys. Rev. Lett.* 126, 025503. <http://dx.doi.org/10.1103/PhysRevLett.126.025503>.
- Brodnik, N.R., Hsueh, C.-J., Faber, K.T., Bourdin, B., Ravichandran, G., Bhattacharya, K., 2020. Guiding and trapping cracks with compliant inclusions for enhancing toughness of brittle composite materials. *J. Appl. Mech.* 87 (3), 031018. <http://dx.doi.org/10.1115/1.4045682>.
- Camacho, G.T., Ortiz, M., 1996. Computational modelling of impact damage in brittle materials. *Int. J. Solids Struct.* 33 (20), 2899–2938.
- Chambolle, A., 2004. An approximation result for special functions with bounded deformation. *J. Math. Pures Appl.* 83 (7), 929–954. <http://dx.doi.org/10.1016/j.matpur.2004.02.004>.
- Chambolle, A., 2005. Addendum to an approximation result for special functions with bounded deformation. [J. Math. Pures Appl.(9) 83 (7)(2004) 929–954]: the N-dimensional case. *J. Math. Pures Appl.* 84 (1), 137–145.
- Clegg, W., Kendall, K., Alford, N.M., Button, T., Birchall, J., 1990. A simple way to make tough ceramics. *Nature* 347 (6292), 455–457.
- Comninou, M., 1977. The interface crack. *J. Appl. Mech.* 44 (4), 631–636.
- Cook, T., Erdogan, F., 1972. Stresses in bonded materials with a crack perpendicular to the interface. *Internat. J. Engrg. Sci.* 10 (8), 677–697.
- Cook, J., Gordon, J.E., 1964. A mechanism for the control of crack propagation in all-brittle systems. *Proc. R. Soc. Lond. Ser. A* 282 (1391), 508–520.
- Currey, J., 1977. Mechanical properties of mother of pearl in tension. *Proc. R. Soc. Lond. Ser. B* 196 (1125), 443–463.
- Dal Maso, G., 1993. An Introduction to  $\Gamma$ -Convergence. In: *Progress in Nonlinear Differential Equations and Their Applications*, vol. 8, Springer Science & Business Media, New York.
- Delale, F., Erdogan, F., 1988. Interface crack in a nonhomogeneous elastic medium. *Internat. J. Engrg. Sci.* 26 (6), 559–568.
- Dundurs, J., 1969. Edge-bonded dissimilar orthogonal elastic wedges. *J. Appl. Mech.* 36 (3), 650–652.
- Edgar, G., 2008. Measure, Topology, and Fractal Geometry, second ed. In: *Undergraduate Texts in Mathematics*, Springer.
- Evans, L.C., Garipey, R.F., 2015. Measure Theory and Fine Properties of Functions, revised ed. In: *Textbooks in Mathematics*, CRC Press.
- Evans, A., Suo, Z., Wang, R., Aksay, I., He, M., Hutchinson, J., 2001. Model for the robust mechanical behavior of nacre. *J. Mater. Res.* 16 (09), 2475–2484.
- Federer, H., 1996. Geometric Measure Theory. In: *Classics in Mathematics*, Springer-Verlag.
- Francfort, G.A., Larsen, C.J., 2003. Existence and convergence for quasi-static evolution in brittle fracture. *Comm. Pure Appl. Math.* 56 (10), 1465–1500. <http://dx.doi.org/10.1002/cpa.3039>.
- Francfort, G.A., Marigo, J.-J., 1998. Revisiting brittle fracture as an energy minimization problem. *J. Mech. Phys. Solids* 46 (8), 1319–1342.
- Griffith, A.A., 1921. The phenomena of rupture and flow in solids. *Philos. Trans. R. Soc. Lond. Ser. A* 221, 163–198.
- Hansen-Dörr, A.C., Dammaß, F., de Borst, R., Kästner, M., 2020. Phase-field modeling of crack branching and deflection in heterogeneous media. *Eng. Fract. Mech.* 232, 107004. <http://dx.doi.org/10.1016/j.engfracmech.2020.107004>.
- Hansen-Dörr, A.C., de Borst, R., Hennig, P., Kästner, M., 2019. Phase-field modelling of interface failure in brittle materials. *Comput. Methods Appl. Mech. Engrg.* 346, 25–42. <http://dx.doi.org/10.1016/j.cma.2018.11.020>.
- He, M.-Y., Hutchinson, J.W., 1989. Kinking of a crack out of an interface. *J. Appl. Mech.* 56 (2), 270–278.
- Hossain, M., Hsueh, C.-J., Bourdin, B., Bhattacharya, K., 2014. Effective toughness of heterogeneous media. *J. Mech. Phys. Solids* 71, 15–32.
- Hsueh, C.-J., Avellar, L., Bourdin, B., Ravichandran, G., Bhattacharya, K., 2018. Stress fluctuation, crack renucleation and toughening in layered materials. *J. Mech. Phys. Solids* 120, 68–78. <http://dx.doi.org/10.1016/j.jmps.2018.04.011>.
- Huajian, G., 1991. Fracture analysis of nonhomogeneous materials via a moduli-perturbation approach. *Int. J. Solids Struct.* 27 (13), 1663–1682.
- Hughes, T.J., 2000. The Finite Element Method: Linear Static and Dynamic Finite Element Analysis. Courier Corporation, New York.
- Hutchinson, J.W., Suo, Z., 1991. Mixed mode cracking in layered materials. *Adv. Appl. Mech.* 29, 63–191.
- Jackson, A., Vincent, J., Turner, R., 1988. The mechanical design of nacre. *Proc. R. Soc. Lond. Ser. B* 234 (1277), 415–440.
- Jaslow, C.R., 1990. Mechanical properties of cranial sutures. *J. Biomech.* 23 (4), 313–321.
- Karma, A., Kessler, D.A., Levine, H., 2001. Phase-field model of mode III dynamic fracture. *Phys. Rev. Lett.* 87, 045501. <http://dx.doi.org/10.1103/PhysRevLett.87.045501>.
- Kuhn, C., Müller, R., 2010. A continuum phase field model for fracture. *Eng. Fract. Mech.* 77 (18), 3625–3634.
- Lange, F., 1970. The interaction of a crack front with a second-phase dispersion. *Phil. Mag.* 22 (179), 0983–0992.
- Lee, N., Horstemeyer, M., Rhee, H., Nabors, B., Liao, J., Williams, L.N., 2014. Hierarchical multiscale structure–property relationships of the red-bellied woodpecker (*Melanerpes carolinus*) beak. *J. R. Soc. Interface* 11 (96), 20140274.
- Li, Y., Ortiz, C., Boyce, M.C., 2011. Stiffness and strength of suture joints in nature. *Phys. Rev. E* 84 (6), 062904.
- Li, Y., Ortiz, C., Boyce, M.C., 2013. A generalized mechanical model for suture interfaces of arbitrary geometry. *J. Mech. Phys. Solids* 61 (4), 1144–1167.
- Lim, R., Pro, J., Begley, M., Utz, M., Petzold, L., 2016. High-performance simulation of fracture in idealized ‘brick and mortar’ composites using adaptive Monte Carlo minimization on the GPU. *Int. J. High Perform. Comput. Appl.* 30 (2), 186–199.
- Lin, E., Li, Y., Ortiz, C., Boyce, M.C., 2014. 3D printed, bio-inspired prototypes and analytical models for structured suture interfaces with geometrically-tuned deformation and failure behavior. *J. Mech. Phys. Solids* 73, 166–182.
- Miehe, C., Hofacker, M., Welschinger, F., 2010a. A phase field model for rate-independent crack propagation: Robust algorithmic implementation based on operator splits. *Comput. Methods Appl. Mech. Engrg.* 199 (45), 2765–2778. <http://dx.doi.org/10.1016/j.cma.2010.04.011>.
- Miehe, C., Welschinger, F., Hofacker, M., 2010b. Thermodynamically consistent phase-field models of fracture: Variational principles and multi-field FE implementations. *Internat. J. Numer. Methods Engrg.* 83 (10), 1273–1311.
- Mirkhalaf, M., Dastjerdi, A.K., Barthelat, F., 2014. Overcoming the brittleness of glass through bio-inspiration and micro-architecture. *Nature Commun.* 5.
- Moës, N., Dolbow, J., Belytschko, T., 1999. A finite element method for crack growth without remeshing. *Internat. J. Numer. Methods Engrg.* 46 (1), 131–150.
- Moës, N., Gravouil, A., Belytschko, T., 2002. Non-planar 3D crack growth by the extended finite element and level sets–part I: Mechanical model. *Internat. J. Numer. Methods Engrg.* 53 (11), 2549–2568.
- Mower, T.M., Argon, A.S., 1995. Experimental investigations of crack trapping in brittle heterogeneous solids. *Mech. Mater.* 19 (4), 343–364.
- Neilson, J.R., George, N.C., Murr, M.M., Seshadri, R., Morse, D.E., 2014. Mesostructure from hydration gradients in demosponge biosilica. *Chem. Eur. J.* 20 (17), 4956–4965.
- Peerlings, R.H.J., De Borst, R., Brekelmans, W.A.M., De Vree, J.H.P., 1996. Gradient enhanced damage for quasi-brittle materials. *Internat. J. Numer. Methods Engrg.* 39 (19), 3391–3403. [http://dx.doi.org/10.1002/\(SICI\)1097-0207\(19961015\)39:19<3391::AID-NME7>3.0.CO;2-D](http://dx.doi.org/10.1002/(SICI)1097-0207(19961015)39:19<3391::AID-NME7>3.0.CO;2-D).
- Pro, J., Lim, R., Petzold, L., Utz, M., Begley, M., 2015. GPU-based simulations of fracture in idealized brick and mortar composites. *J. Mech. Phys. Solids* 80, 68–85.
- Rabiei, R., Bekah, S., Barthelat, F., 2012. Nacre from mollusk shells: Inspiration for high-performance nanocomposites. In: John, M., Thomas, S. (Eds.), *Natural Polymers*. In: *Green Chemistry*, vol. 2, Royal Society of Chemistry, pp. 113–146.
- Rice, J., 1988. Elastic fracture mechanics concepts for interfacial cracks. *J. Appl. Mech.* 55 (1), 98–103.
- Ritchie, R., 2011. The conflicts between strength and toughness. *Nature Mater.* 10 (11), 817–822.
- Shen, Y., Wu, C., Wan, Y., 2017. Universal meshes for a branched crack. *Finite Elements in Analysis and Design* 129, 53–62.



- Sukumar, N., Dolbow, J., Moës, N., 2015. Extended finite element method in computational fracture mechanics: A retrospective examination. *Int. J. Fract.* 196 (1–2), 189–206.
- Suresh, S., 1985. Fatigue crack deflection and fracture surface contact: Micromechanical models. *Metall. Trans. A* 16 (1), 249–260.
- Tattersall, H.G., Tappin, G., 1966. The work of fracture and its measurement in metals, ceramics and other materials. *J. Mater. Sci.* 1 (3), 296–301.
- Tvergaard, V., Hutchinson, J.W., 1996. On the toughness of ductile adhesive joints. *J. Mech. Phys. Solids* 44 (5), 789–800.
- Unnikrishna Pillai, A., Behera, A.K., Rahaman, M.M., 2023. Combined diffused material interface and hybrid phase-field model for brittle fracture in heterogeneous composites. *Eng. Fract. Mech.* 277, 108957. <http://dx.doi.org/10.1016/j.engfracmech.2022.108957>.
- Veljkovic, J., 2005. The crack kinking out of an interface. *Theor. Appl. Mech.* 32 (3), 208–221.
- Vijaykumar, K., 2019. A Variational Mechanics Theory for Modeling the Evolution of Crack Networks in Composite Materials with Brittle Interfaces (Ph.D. thesis). Brown University.
- Vol'pert, A., Hudjaev, S., 1985. Analysis in Classes of Discontinuous Functions and Equations of Mathematical Physics. In: *Mechanics: Analysis*, vol. 8, Martinus Nijhoff Publishers.
- Wan, Y., Xue, T., Shen, Y., 2019. The successive node snapping scheme: A method to obtain conforming meshes for an evolving curve in 2D and 3D. *Finite Elements in Analysis and Design* 153, 1–21.
- Wang, X., Wiens, M., Schröder, H.C., Hu, S., Mugnaioli, E., Kolb, U., Tremel, W., Pisignano, D., Müller, W.E., 2010. Morphology of sponge spicules: Silicatein a structural protein for bio-silica formation. *Adv. Eng. Mater.* 12 (9), B422–B437.
- Weaver, J.C., Milliron, G.W., Allen, P., Miserez, A., Rawal, A., Garay, J., Thurner, P.J., Seto, J., Mayzel, B., Friesen, L.J., et al., 2010. Unifying design strategies in demopong and hexactinellid skeletal systems. *J. Adhes.* 86 (1), 72–95.
- Weaver, J.C., Pietrasanta, I., Hedin, N., Chmelka, B.F., Hansma, P.K., Morse, D.E., et al., 2003. Nanostructural features of demopong biosilica. *J. Struct. Biol.* 144 (3), 271–281.
- Wegst, U.G., Bai, H., Saiz, E., Tomsia, A.P., Ritchie, R.O., 2015. Bioinspired structural materials. *Nature Mater.* 14 (1), 23–36.
- Xu, G., Bower, A., Ortiz, M., 1998. The influence of crack trapping on the toughness of fiber reinforced composites. *J. Mech. Phys. Solids* 46 (10), 1815–1833.
- Xu, X.-P., Needleman, A., 1994. Numerical simulations of fast crack growth in brittle solids. *J. Mech. Phys. Solids* 42 (9), 1397–1434.
- Yoshioka, K., Mollaali, M., Kolditz, O., 2021. Variational phase-field fracture modeling with interfaces. *Comput. Methods Appl. Mech. Engrg.* 384, 113951. <http://dx.doi.org/10.1016/j.cma.2021.113951>.
- Zavattieri, P., Hector Jr., L., Bower, A., 2007. Determination of the effective mode-I toughness of a sinusoidal interface between two elastic solids. *Int. J. Fract.* 145 (3), 167–180.
- Zhou, Q., Wei, Y., Zhou, Y., Yang, L., 2022. An interface-width-insensitive cohesive phase-field model for fracture evolution in heterogeneous materials. *Int. J. Solids Struct.* 256, 111980. <http://dx.doi.org/10.1016/j.ijsolstr.2022.111980>.
- Zlotnikov, I., Shilo, D., Dauphin, Y., Blumtritt, H., Werner, P., Zolotoyabko, E., Fratzl, P., 2013. In situ elastic modulus measurements of ultrathin protein-rich organic layers in biosilica: Towards deeper understanding of superior resistance to fracture of biocomposites. *RSC Adv.* 3 (17), 5798–5802.